

Pathogenic hypothalamic extracellular matrix promotes metabolic disease

<https://doi.org/10.1038/s41586-024-07922-y>

Received: 26 May 2022

Accepted: 7 August 2024

Published online: 18 September 2024

Open access

 Check for updates

Cait A. Beddows¹, Feiyue Shi¹, Anna L. Horton^{2,3}, Sagar Dalal⁴, Ping Zhang⁵, Chang-Chun Ling⁶, V. Wee Yong⁶, Kim Loh⁷, Ellie Cho⁸, Chris Karagiannis⁹, Adam J. Rose¹⁰, Magdalene K. Montgomery¹, Paul Gregorevic^{9,11}, Matthew J. Watt¹, Nicolle H. Packer⁴, Benjamin L. Parker¹, Robyn M. Brown^{2,3}, Edward S. X. Moh⁴ & Garron T. Dodd¹✉

Metabolic diseases such as obesity and type 2 diabetes are marked by insulin resistance^{1,2}. Cells within the arcuate nucleus of the hypothalamus (ARC), which are crucial for regulating metabolism, become insulin resistant during the progression of metabolic disease^{3–8}, but these mechanisms are not fully understood. Here we investigated the role of a specialized chondroitin sulfate proteoglycan extracellular matrix, termed a perineuronal net, which surrounds ARC neurons. In metabolic disease, the perineuronal net of the ARC becomes augmented and remodelled, driving insulin resistance and metabolic dysfunction. Disruption of the perineuronal net in obese mice, either enzymatically or with small molecules, improves insulin access to the brain, reversing neuronal insulin resistance and enhancing metabolic health. Our findings identify ARC extracellular matrix remodelling as a fundamental mechanism driving metabolic diseases.

Insulin resistance is intimately linked to extracellular matrix (ECM) remodelling in peripheral tissues, where excessive ECM deposition, a phenomenon termed fibrosis, impairs insulin action and signalling^{9,10}. Traditionally, fibrosis has been viewed as occurring only in peripheral tissues. However, remodelling of ECM within the brain has been observed following acute brain injury and in several neurological diseases¹¹.

Recent work has identified the formation of perineuronal nets (PNNs), a unique ECM subtype, around neurons that express agouti-related peptide (AgRP) in the ARC during neuronal maturation^{12,13}. This PNN formation directly influences AgRP function, as its loss leads to increased fibre density and changes in cell numbers¹⁴. The innate relationship between the PNN and ARC cells may underscore a fundamental mechanism intrinsic to the neuroendocrine axis governing metabolism. The relevance of the ECM within the context of metabolism has been further emphasized by recent observations that the ECM in the median eminence, a region adjacent to the ARC, can be transiently remodelled in response to nutritional status¹⁵. Given the association between fibrosis and cellular dysfunction in the periphery, ECM remodelling in the ARC could represent a completely unexplored mechanism in the pathogenesis of metabolic disease.

Here we identify that during the development of metabolic disease, the ARC ECM becomes augmented and remodelled, impeding insulin penetrance and resulting in insulin resistance. By disassembling the pathogenic ECM in the ARC of obese and type 2 diabetic mice, we promote disease remission and causally implicate ARC ECM remodelling as a disease mechanism and therapeutic target in metabolic disease.

Neurofibrosis develops in metabolic disease

PNN was detected throughout the mouse mediobasal hypothalamus (Fig. 1a–c and Extended Data Fig. 1a–f) by *Wisteria floribunda* lectin (WFA) staining. We observed prominent PNN staining in the ARC (Fig. 1a–c and Extended Data Fig. 1a–f) with notable but significantly less PNN staining within the adjacent ventromedial hypothalamus (VMH) (Extended Data Fig. 1i–k). There was a robust increase in the area and intensity of PNN staining within the ARC of diet-induced obese (DIO) mice fed a high-fat, high-sugar (HFHS) diet for 12 weeks (Fig. 1a–c and Extended Data Fig. 1a–f). Significant increases in PNN abundance occurred within 4 weeks of HFHS feeding and PNN was further increased at 8 and 12 weeks (Fig. 1d,e and Extended Data Fig. 1l). This augmentation was associated with the development of key pathophysiological hallmarks of metabolic disease (Extended Data Fig. 1m–o). Remodelling of the PNN following HFHS diet was not observed in the retrosplenial granular cortex (RSG) or the VMH (Extended Data Fig. 1g–k), suggesting that obesity-driven ECM remodelling occurs specifically within the ARC. To evaluate whether the chondroitin sulfate glycosaminoglycan (CS-GAG) chain composition of the ARC PNN is remodelled, we performed quantitative analysis of enzymatically released chondroitin sulfate disaccharides from the ARC PNN and observed a significant increase in CS-GAG abundances (Fig. 1f), which is consistent with the augmentation in the PNN detected immunohistochemically. This ECM remodelling was a consistent pathological feature of several independent dietary and genetic murine models of metabolic disease

¹Department of Anatomy and Physiology, The University of Melbourne, Melbourne, Victoria, Australia. ²Department of Biochemistry and Pharmacology, The University of Melbourne, Melbourne, Victoria, Australia. ³Florey Institute of Neuroscience and Mental Health, The University of Melbourne, Melbourne, Victoria, Australia. ⁴ARC Centre of Excellence in Synthetic Biology, School of Natural Sciences, Macquarie University, Sydney, New South Wales, Australia. ⁵Department of Chemistry, University of Calgary, Calgary, Alberta, Canada. ⁶Department of Clinical Neurosciences and the Hotchkiss Brain Institute, Cumming School of Medicine, University of Calgary, Calgary, Alberta, Canada. ⁷St Vincent's Institute of Medical Research, Melbourne, Victoria, Australia.

⁸Biological Optical Microscopy Platform, The University of Melbourne, Melbourne, Victoria, Australia. ⁹Centre for Muscle Research, The University of Melbourne, Melbourne, Victoria, Australia.

¹⁰Department of Biochemistry and Molecular Biology, Monash Biomedicine Discovery Institute, Monash University, Melbourne, Victoria, Australia. ¹¹Department of Neurology, The University of Washington School of Medicine, Seattle, Washington, USA. ✉e-mail: garron.dodd@unimelb.edu.au

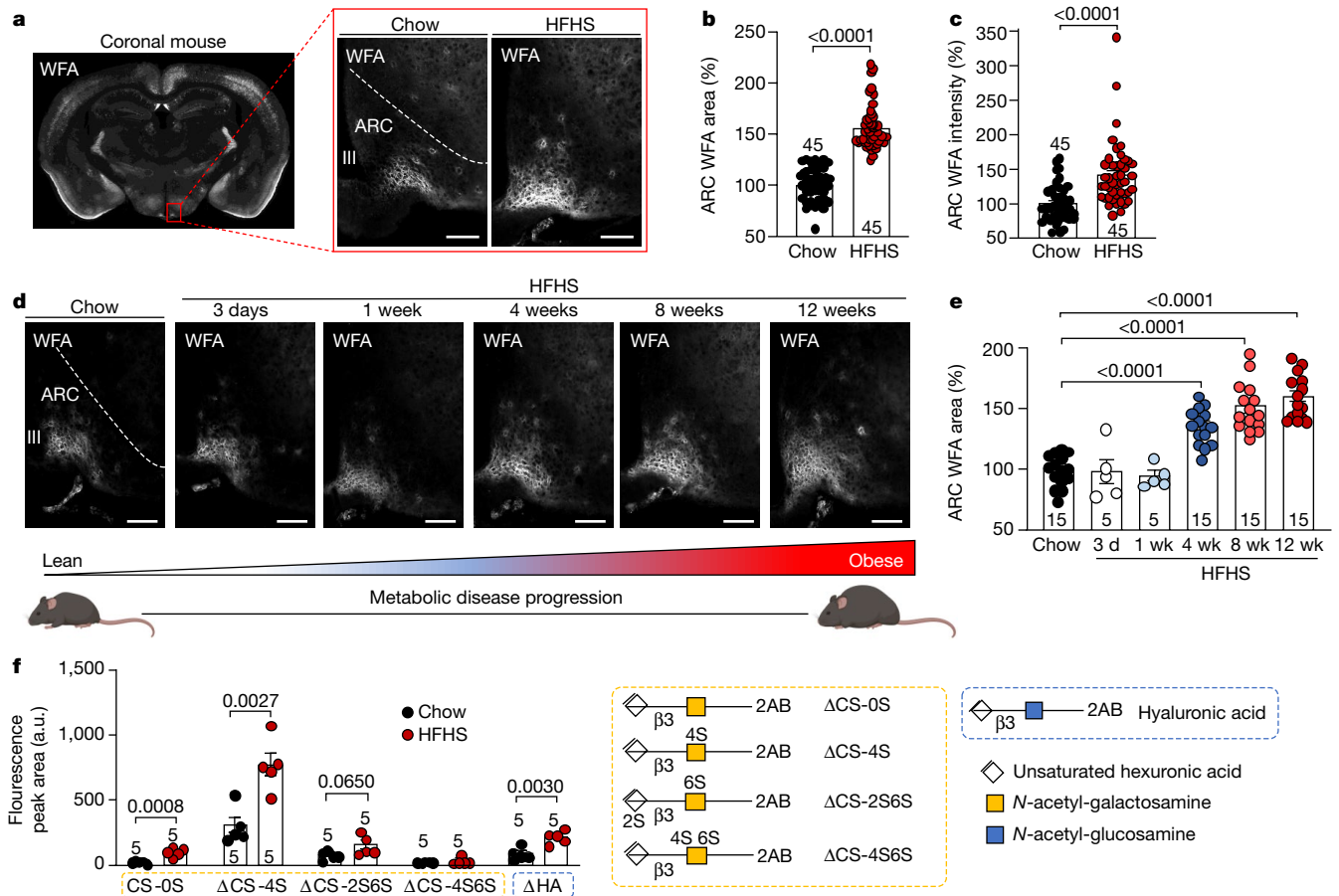


Fig. 1 | Obesity drives neurofibrosis within the ARC. **a–e**, Aged-matched C57BL/6J mice were fed either a chow or an HFHS diet for 0 days, 3 days or 1, 4, 8 or 12 weeks and brains were processed for WFA staining. **a**, Whole-brain coronal section, showing WFA staining in the ARC. **b,c**, Quantification of WFA-stained area (**b**) and intensity (**c**) in the ARC of 12-week HFHS-fed mice. **d,e**, WFA staining (**d**) and quantification of WFA-stained area (**e**) in mice fed chow or HFHS diet for 0 days, 3 days (**d**) or 1, 4, 8 or 12 weeks (**wk**). **f**, ARC homogenates from 12-week HFHS-fed or chow-fed C57BL/6J mice were analysed using zwitterionic hydrophilic interaction liquid chromatography to quantify the abundance of CS-GAG and hyaluronic acid (β 1-3-linked disaccharides with

various sulfate positions: 0S, non-sulfated; 2S, sulfated unsaturated hexuronic acid; 4S, 6S, sulfated *N*-acetyl-galactosamine) with 2-aminobenzamide fluorescently labelled disaccharides from enzymatically depolymerized GAG chains. Data are mean \pm s.e.m. *n* value represent independent mice and are shown on or above each bar plot; representative of at least three independent experiments. Two-tailed *t*-test (**b,c,f**) and one-way ANOVA with Dunnett's multiple comparisons (**e**). Scale bars, 100 μ m. a.u., arbitrary units; 2-AB, 2-aminobenzamide; III, third ventricle; CS, chondroitin sulfate; GAG, glycosaminoglycan, HA, hyaluronic acid.

(Extended Data Fig. 1p–z). As the pathological augmentation and remodelling of ECM within peripheral tissue is termed fibrosis, we refer to this phenomenon of excessive ARC PNN deposition and remodelling as neurofibrosis.

Aggrecan is a key CSPG component of neurofibrosis

Exploring the compositional remodelling of the ARC PNN in neurofibrosis (Supplementary Fig. 1a), we noted heterogeneous staining of hyaluronic acid throughout the brain parenchyma with near-complete co-localization with WFA in the ARC, and an increase in both the ARC staining area and intensity in DIO mice (Supplementary Fig. 1b–e). A corresponding increase in the abundance of hyaluronic and proteoglycan link proteins (HAPLN1) and the chondroitin sulfate proteoglycan (CSPG) cross-linking glycoprotein tenascin C (Supplementary Fig. 1g–j, l–o) was also observed in the ARC of HFHS-fed mice. Notably, these ECM components were widely expressed throughout the hypothalamus, indicating their functionality in ECMs outside the ARC PNN (Extended Data Fig. 1f, k, p).

We next immunolabelled major CSPG components expressed in ECMs elsewhere in the brain¹⁶ (Supplementary Fig. 1a). Although all CSPG components that we assessed were present within the ARC to

some degree, it was aggrecan that predominantly co-localized with WFA in the ARC under both chow-fed and HFHS-fed conditions, with other CSPG components exhibiting a distinct spatial pattern from the WFA-labelled PNN in the ARC (Extended Data Fig. 2a–e and Supplementary Fig. 2e, j, o, t). Obesity promoted increased versican, neurocan, brevican and aggrecan within the ARC (Extended Data Fig. 2a–d and Supplementary Fig. 2a–d, f–i, k–n, p–s), with the obesity-driven augmentation of aggrecan occurring within a similar period to that of WFA-labelled PNN (Extended Data Fig. 2f, g and Supplementary Fig. 2u). Together, these results demonstrate that obesity promotes augmentation of most major ECM components however aggrecan is a predominate CSPG species underpinning neurofibrosis.

Neurofibrosis develops around AgRP neurons

The ARC contains two metabolically relevant neuronal populations: AgRP neurons and pro-opiomelanocortin (POMC) neurons. Using *Npy*-GFP and *Pomc*-GFP mice, we identified that under chow-fed conditions, 45 \pm 13% of AgRP neurons and 24 \pm 9% of POMC neurons (Extended Data Fig. 2h, i, l, m) in the ARC were ensheathed within the PNN. This number significantly increases specifically for AgRP neurons during the progression of metabolic disease alongside an

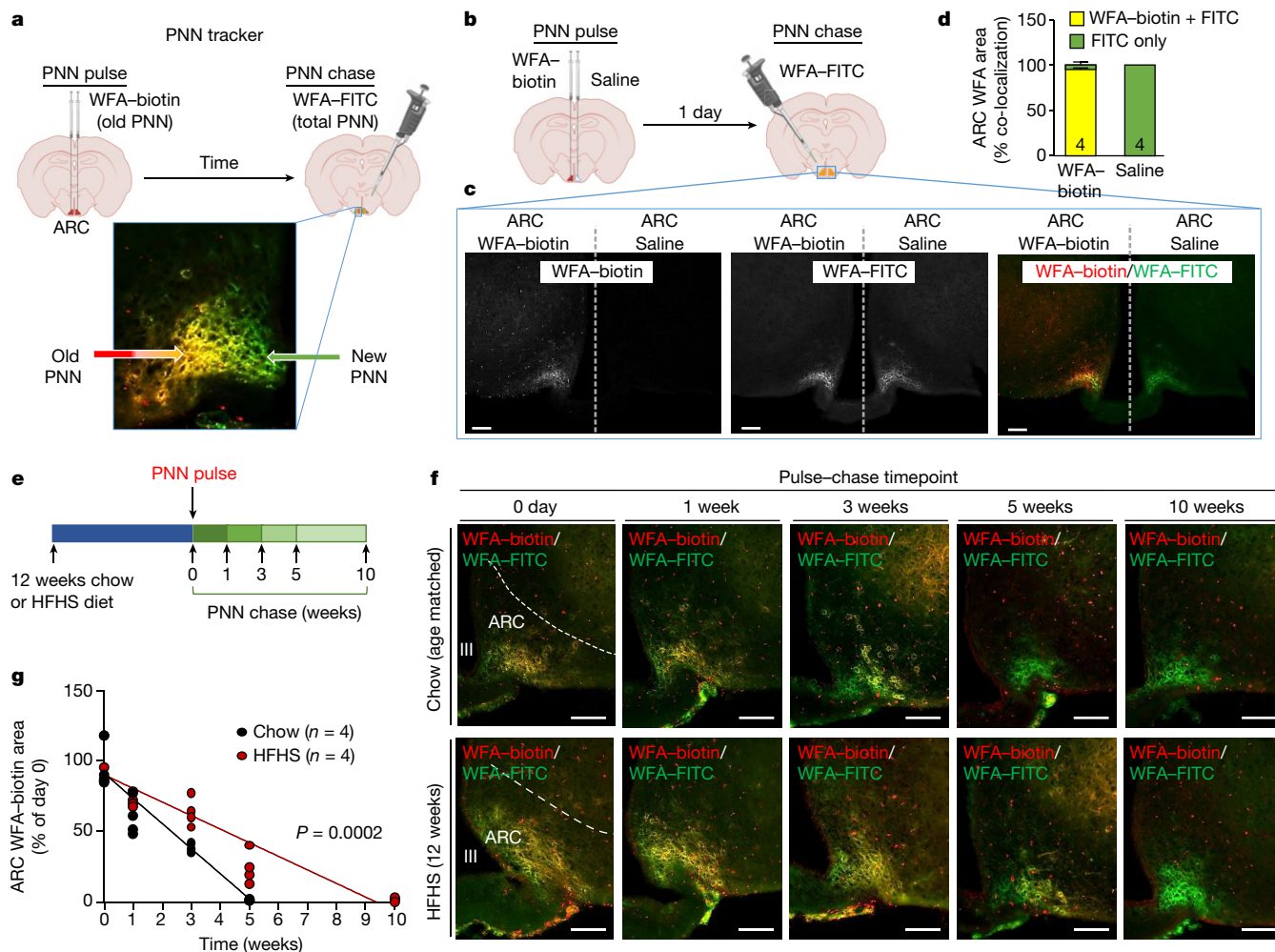


Fig. 2 | Attenuated PNN turnover in the ARC drives neurofibrosis. **a**, Schematic overview of the PNN tracker method. **b,c**, Unilateral administration of WFA-biotin or saline into the ARC of 8-week-old C57BL6/J mice (**b**); one day after injection, brains were processed for immunohistochemistry to monitor for WFA-biotin and WFA-FITC. **d**, Quantification of WFA-stained area within the ARC. **e**, Twelve-week DIO or age-matched 12-week chow-fed C57BL6/J male mice received

bilateral WFA-biotin injections into the ARC. Brains were extracted at 0 days or 1, 3, 5 or 10 weeks after injection and analysed for the presence of WFA-biotin and WFA-FITC presence. **f,g**, PNN turnover within the ARC was imaged (**f**) and quantified (**g**; simple linear regression) over time. Data are mean \pm s.e.m. *n* represents biologically independent samples; representative of at least two independent experiments. Scale bars, 100 μ m.

enhancement of surrounding WFA and aggrecan staining, independent of changes in neuron numbers (Extended Data Fig. 2h-r). Collectively, these results demonstrate that neurofibrosis develops around AgRP neurons in the ARC during the development of metabolic disease.

A method to determine site-specific PNN turnover

PNNs are described as exhibiting slow biological turnover rates and persist in adult tissues for several months to years¹⁷, yet our results demonstrate a comparatively rapid remodelling and augmentation of the ARC PNN following exposure to an obesogenic diet (Fig. 1). To experimentally determine the PNN turnover rate in vivo, we developed PNN tracker, a pulse-chase approach utilizing a stereotaxic injection of biotinylated WFA (WFA-biotin) to pulse and label the PNN in a brain region of interest (Fig. 2a). Following an in vivo incubation period, brains are extracted and processed ex vivo for the presence of WFA-biotin to chase the labelled PNN remaining from the time of injection (day 0) and co-stained with WFA-FITC to reveal the total PNN expression at the time of the chase (Fig. 2a). To validate this approach as a bona fide tracker of PNN turnover, we unilaterally pulsed the ARC of adult chow-fed mice with either WFA-biotin or saline, and chased expression

one day later (Fig. 2b,c). We identified near-complete co-localization of pulsed WFA-biotin signal with WFA-FITC (total PNN), suggesting that PNN tracker faithfully labels PNNs in the ARC in vivo (Fig. 2d). Speckles of WFA-positive signal outside the ARC represents WFA-biotin leakage into the circulation and binding to PNN expressed in blood vessels (Fig. 2c). To validate whether the pulsed WFA-biotin signal faithfully binds and labels PNN present at the time of injection, we bilaterally pulsed the ARC with WFA-biotin and three days later digested the PNN in the ARC with chondroitinase ABC (chABC), an enzyme that specifically digests PNNs (Extended Data Fig. 3a-d). Enzymatic digestion of the pulsed WFA-biotin-bound PNN was completely abolished following chABC treatment compared with vehicle (Extended Data Fig. 3b-d), indicating that WFA-biotin binds to PNN components that are present only at the time of the pulse injection.

ARC PNN exhibits dynamic and rapid turnover

Analysis using PNN tracker showed that the PNN in the ARC of chow-fed mice exhibits a turnover period of approximately five weeks (Fig. 2e-g and Extended Data Fig. 3m-p). Radiotracer experiments have previously demonstrated that chondroitin sulfate in the rat brain has a half-life of approximately one week, consistent with the approximately

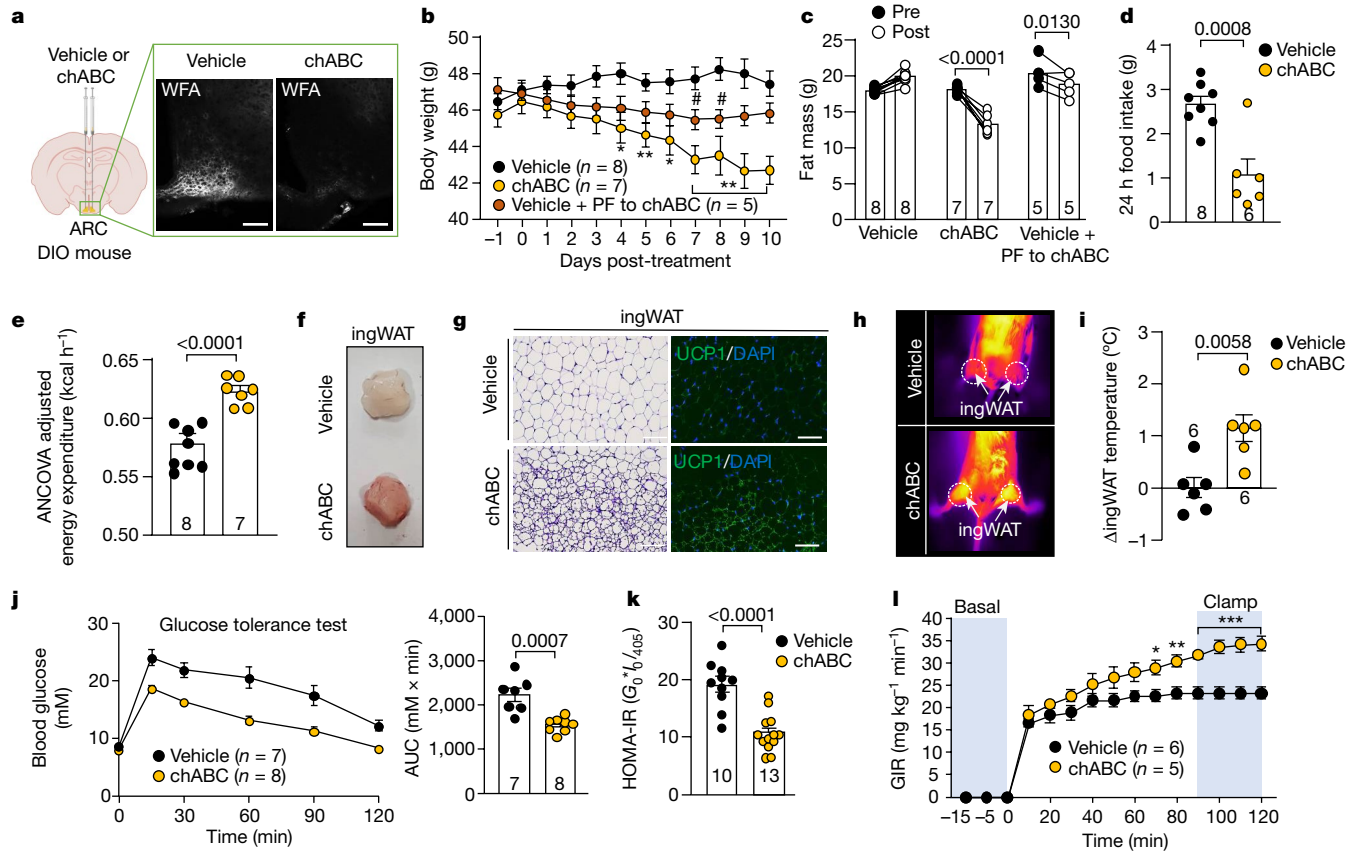


Fig. 3 | Disassembly of neurofibrosis within the ARC promotes the remission of metabolic disease. **a**, C57BL/6J mice on a HFHS diet received bilateral intra-ARC injections of vehicle or chABC. Vehicle-treated mice were pair-fed (PF) to the food intake of chABC-treated mice. **b–k**, Body weight (**b**), adiposity (**c**), food intake (**d**), energy expenditure (**e**), gross morphology of ingWAT (**f**), ingWAT histology and UCP1 immunohistochemistry (**g**), inguinal dermal thermography (**h**) with quantification (**i**), glucose tolerance (**j**) and HOMA-IR (**k**) for mice treated as described in **a**. AUC, area under the curve.

l, Hyperinsulinaemic–euglycaemic clamps were performed in HFHS-fed mice following bilateral injections of vehicle or chABC into the ARC and glucose infusion rate (GIR) was determined. Data are mean \pm s.e.m. Two-way ANOVA with multiple comparisons or repeated-measures (**b**, **c**, **l**) and two-tailed *t*-test (**d**, **e**, **i**–**k**). *n* represents biologically independent samples; representative of at least two independent experiments. Scale bars, 100 μ m. *P* values compare vehicle to chABC (*), or vehicle to vehicle or pair-fed to chABC (#). ***P* < 0.05, ****P* < 0.01, *****P* < 0.001, ******P* < 0.0001.

40% reduction observed in the ARC one week after pulse injection¹⁷. By contrast, the PNN in the RSG persisted for five weeks, and no degradation was observed in the blood vessels of the adjacent corpus callosum (Extended Data Fig. 3e–l). These findings highlight the uniquely rapid degradation rate of PNN in the ARC and establishes differential ECM turnover across different brain regions.

Reduced PNN turnover in obesity drives neurofibrosis

We hypothesized that neurofibrosis in the ARC results from reduced PNN degradation. To test this, we pulsed WFA–biotin into the ARC of obese mice and chased its expression (Fig. 2e, f and Extended Data Fig. 3o, p). The PNN degradation rate in obese mice was significantly slower than in lean mice (2.6% per day versus 0.1% per day), with WFA–biotin persisting in the ARC of obese mice for up to 10 weeks—twice as long as in lean mice (Fig. 2g and Extended Data Fig. 3m–o).

To elucidate the molecular mechanism underlying obesity-driven alterations in the PNN turnover we quantified the gene expression of established ECM synthesis and degradation enzymes in the mediobasal hypothalamus of lean versus obese mice. We observed significantly reduced expression of several key ECM proteases and increased expression of their inhibitors in obese mice (Extended Data Fig. 3q). Together, these results show that neurofibrosis is driven by attenuated PNN degradation and illustrate the transfiguration of the ARC PNN during the development of metabolic disease.

Abrogating ARC neurofibrosis protects against obesity

To determine the role of ARC neurofibrosis in metabolic disease, we used chABC to selectively disassemble the PNN within the ARC of DIO mice. This treatment promoted progressive weight loss, reduced adiposity and decreased caloric intake (Fig. 3a–d and Extended Data Fig. 4a–d). Pair-fed vehicle-treated mice did not exhibit similar reductions of body weight or adiposity (Fig. 3b, c), indicating that weight loss from abrogation of neurofibrosis cannot be solely attributed to reduced feeding. Indirect calorimetry revealed increased whole-body energy expenditure and oxygen consumption, with no changes in substrate partitioning or ambulatory activity (Fig. 3e and Extended Data Fig. 4e–j) in chABC-treated mice. Additionally, enhanced thermogenesis was observed in inguinal white adipose tissue (ingWAT) and brown adipose tissue (BAT) depots (Fig. 3f–i and Extended Data Fig. 4k).

Abrogation of ARC neurofibrosis also improved glucose homeostasis, reducing circulating insulin and HOMA-IR (homeostatic model assessment of insulin resistance—a measure of whole-body insulin resistance; Fig. 3j, k and Extended Data Fig. 4l, m). Notably, these improvements occurred before there were significant changes in body weight, indicating a direct effect of neurofibrosis abrogation on glucose metabolism. Hyperinsulinaemic–euglycaemic clamps showed increased glucose infusion rates (GIR) in chABC-treated mice, reflecting improved whole-body insulin sensitivity (Fig. 3l and Extended Data Fig. 4n). This enhanced insulin sensitivity was linked to reduced endogenous glucose

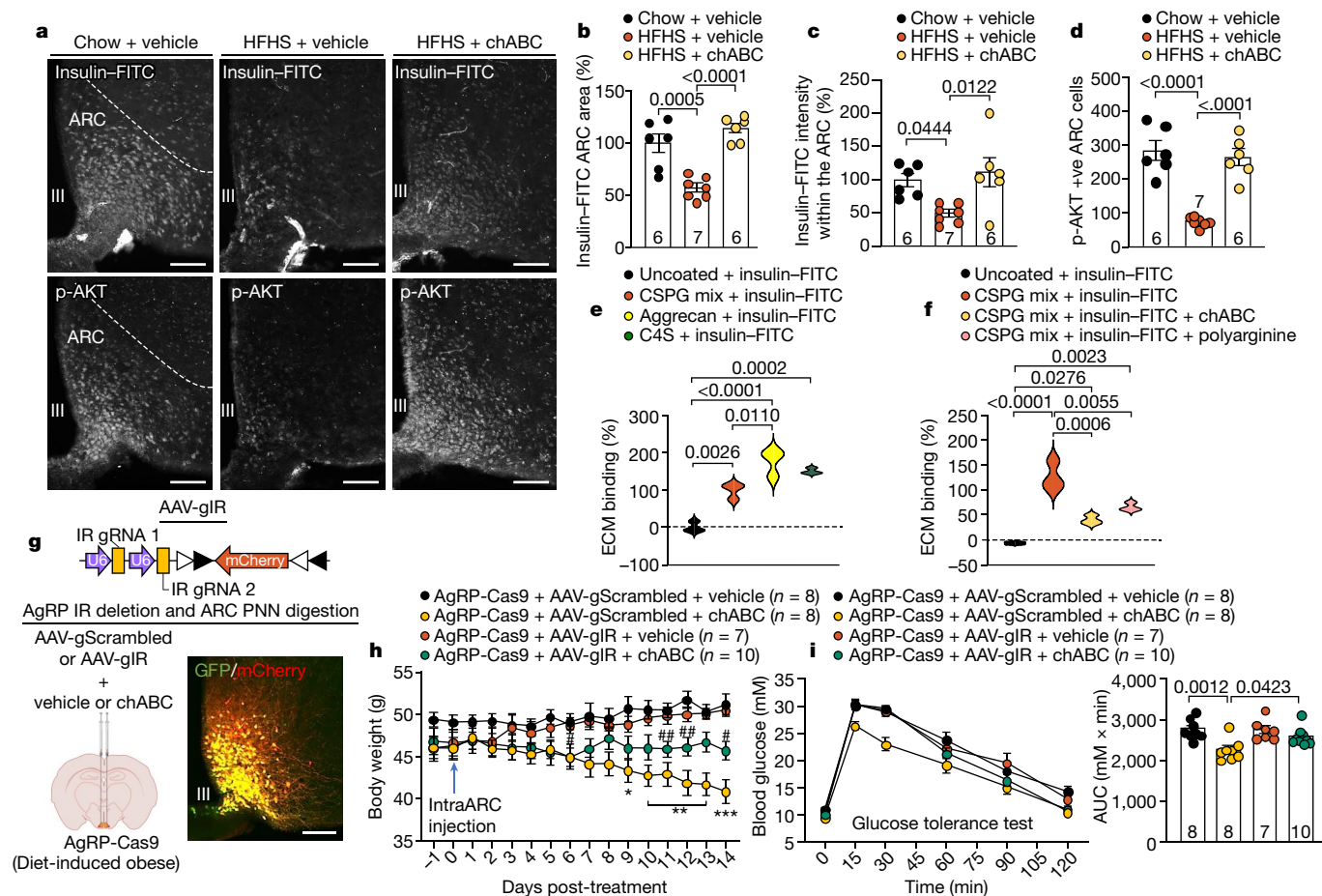


Fig. 4 | Neurofibrosis in obesity promotes ARC insulin resistance.

a, C57BL/6J mice fed a HFHS diet received bilateral intra-ARC injections of vehicle or chABC. **b–d**, Insulin-FITC area (**b**), intensity (**c**) and insulin-FITC induced AKT phosphorylation (**d**) within the ARC were quantified four days post-injection. **e, f**, Insulin-FITC binding to CSPG components—CSPG mix, aggrecan or C4S (**e**) and in the presence of chABC or polyarginine (**f**)—was assessed *in vitro*. **g**, Twelve-week HFHS-fed AgRP-Cas9 mice injected with AAV expressing scrambled (AAV-gScrambled) or insulin receptor (AAV-gIR) sgRNA

into the ARC. ARC targeting was confirmed by *AgRP*-GFP and mCherry immunofluorescence. IR, insulin receptor. **h, i**, One week later, mice received bilateral injections of vehicle or chABC, and body weight (**h**) and glucose tolerance (**i**) were measured. Results are mean \pm s.e.m. Two-way ANOVA with Tukey’s multiple comparisons test (**h**) and one-way ANOVA with Tukey’s multiple comparisons (**b–f, i**). *n* represents biologically independent samples; representative of at least two independent experiments. Scale bars, 100 μ m.

production, improved glucose disposal rate and enhanced glucose uptake in skeletal muscle, BAT and ingWAT (Extended Data Fig. 4o–q). The metabolic benefits of neurofibrosis abrogation were recapitulated in genetically severely obese and type 2 diabetic *db/db* mice treated with chABC (Extended Data Fig. 4r–u), further substantiating the causal role of ARC neurofibrosis in the development of metabolic disease. These results demonstrate that ARC neurofibrosis causally contributes to metabolic disease progression and maintenance, affecting hyperphagia, whole-body insulin resistance, adiposity and thermogenesis.

Neurofibrosis impedes ARC insulin entry and signalling

Given the association between fibrosis and insulin resistance in peripheral tissues^{2,9}, we hypothesized that neurofibrosis may impede insulin delivery into the ARC, contributing to insulin resistance. To test this, we bilaterally administered vehicle or chABC into the ARC of 12-week DIO and chow-fed mice and assessed effects on insulin receptor activation (Extended Data Fig. 5a–e and Supplementary Fig. 3a). Insulin-induced AKT phosphorylation on Ser473 (p-AKT) was significantly attenuated in obese mice relative to lean mice. However, disassembly of the ARC PNN in obese mice rapidly ameliorated insulin resistance within ARC neurons, as evidenced by the reinstatement of p-AKT and insulin receptor phosphorylation within the ARC 2 days (before effects on

body weight) and 8 days after chABC injection (Extended Data Fig. 5a–f and Supplementary Fig. 3a).

To determine whether obesity-driven neurofibrosis mechanistically promotes insulin resistance by impeding the access of insulin to neurons within the ARC, we peripherally administered FITC-tagged insulin (insulin-FITC) and quantified its entry and signalling in the ARC (Supplementary Fig. 3b). We observed robust insulin-FITC appearance, internalization and signalling in the ARC of lean mice, an effect that was impaired in obese mice (Fig. 4a–d and Extended Data Fig. 5g–i). Notably, PNN disassembly in the ARC of DIO mice reinstated insulin entry into the ARC and restored insulin signalling (Fig. 4a–d and Extended Data Fig. 5i).

The CSPGs that comprise the ARC PNN are also expressed within the blood–brain barrier (BBB), suggesting that ARC PNN digestion may also modulate BBB function. To investigate whether the improved insulin access following neurofibrosis digestion is a result of changes in BBB-mediated transport, we infused insulin-FITC into the cerebral spinal fluid, bypassing the BBB (Extended Data Fig. 5j). Insulin-FITC entered the ARC of lean mice but was attenuated in DIO mice; this impairment was rescued by PNN disassembly (Extended Data Fig. 5k–n). These results indicate that although PNN digestion may have an effect on insulin transport through the BBB, those effects are not essential to the improved insulin access and signalling observed following attenuation

of neurofibrosis in obesity. Of note, PNN regulation of insulin–FITC access into the ARC is insulin-specific, as similar effects are not seen with FITC alone or with leptin (Extended Data Fig. 5o–v). Consistent with previous work¹⁸, leptin entry into the ARC in obese mice remained intact. Unlike insulin signalling, enzymatic disassembly of the ARC PNN did not restore leptin sensitivity in the ARC, indicating that neurofibrosis does not regulate leptin entry and signalling (Extended Data Fig. 5r–x).

To understand how neurofibrosis affects insulin infiltration and signalling, we conducted an *in vitro* binding assay to examine insulin–PNN interactions. We incubated insulin–FITC for 2 h on plates coated with mixed CSPGs or specific core PNN components, such as aggrecan or chondroitin 4-sulfate (C4S) (Supplementary Fig. 3c). We observed the binding of insulin–FITC to mixed CSPGs, aggrecan and C4S, effects abolished in the presence of chABC or polyarginine, a peptide that neutralizes the negative charge of CSPGs (Fig. 4e,f and Supplementary Fig. 3d–f). These results indicate that the negative charge of glucosaminoglycans (GAGs) in the PNN regulates insulin–PNN interactions.

Insulin-dependent AgRP hyperactivity in neurofibrosis

Obesity and insulin resistance have been shown to increase the intrinsic excitability of AgRP neurons by increasing firing rate and resting membrane potential¹⁹. Removal of PNNs around cortical and brainstem neurons has been found to reduce membrane excitability and firing frequency²⁰. Therefore, we investigated the effect of neurofibrosis on AgRP neuronal function using whole-cell patch clamp electrophysiology. After 12 weeks of HFHS feeding, more than 82% of AgRP neurons fired spontaneously, but this was reduced to 33% when the PNN within the ARC was disassembled with chABC (Extended Data Fig. 6a). Correspondingly, significant reductions in firing frequency and resting membrane potential were observed (Extended Data Fig. 6b–d), indicating that the ARC PNN regulates the electrophysiological properties of AgRP neurons.

Activation of K⁺ channels on AgRP neurons hyperpolarizes the resting membrane potential, leading to reduced firing rates²¹. To investigate whether neurofibrosis modulates K⁺ currents in AgRP neurons, we examined current–voltage relationships in the presence of tetrodotoxin. We observed an upward shift in the current–voltage curve, indicating enhanced K⁺ currents (Extended Data Fig. 6e and Supplementary Fig. 4a). Additionally, several K⁺ channels were upregulated following digestion of ARC PNN in DIO mice (Extended Data Fig. 6f), suggesting that neurofibrosis regulates ARC neuronal signalling. Since insulin typically hyperpolarizes AgRP neurons²², we utilized an insulin receptor antagonist (S961) to assess whether these changes were a result of improved insulin access. The upregulation of K⁺ channels following neurofibrosis abrogation is attenuated by S961, indicating insulin receptor-dependent regulation of neuronal activity following ARC PNN digestion (Extended Data Fig. 6f).

A notable feature of metabolic disease and insulin resistance is increased AgRP antagonism of the melanocortin system within the paraventricular hypothalamus^{23,24} (PVH). We observed significantly increased AgRP peptide innervating the PVH in obese mice compared with lean mice, which was reversed upon neurofibrosis attenuation (Extended Data Fig. 6g,h). This increase in AgRP firing frequency, peptide expression and subsequent increase in AgRP inhibitory tone to the melanocortin circuitry of the PVH may explain how neurofibrosis around AgRP neurons propagates metabolic dysfunction. Overall, these findings demonstrate that the ARC PNN interacts directly with insulin, and neurofibrosis impairs the ability of insulin to access and signal to key neuronal populations, contributing to insulin resistance.

ARC neurofibrosis impairs AgRP insulin signalling

To define whether impaired AgRP insulin receptor signalling causally underpins neurofibrosis-driven metabolic dysfunction, we

generated a mouse model with conditional insulin receptor deletion in AgRP neurons under adult DIO conditions. We used CRISPR gene editing with two single guide RNAs (sgRNAs) targeting proximal regions of exon 2 of the mouse insulin receptor gene (*Insr*), resulting in near-complete ablation of insulin receptor protein expression (Extended Data Fig. 6i–k and Supplementary Fig. 4b,c). An adeno-associated virus (AAV) expressing the two *Insr* sgRNA sequences (AAV-gIR; Fig. 4g) was delivered to AgRP-Cas9 (*AgRP-IRES-Cre;Rosa26-LSL-Cas9-GFP*) mice. Successful CRISPR-mediated disruption of the insulin receptor was confirmed by the presence of an approximately 419-bp PCR product ($\Delta Insr^{CRISPR}$; approximately 82 bp smaller than the product for the wild type (approximately 501 bp)) in the mediobasal hypothalamus of AgRP-Cas9 mice and by impaired insulin signalling within AgRP neurons (Extended Data Fig. 6k and Supplementary Fig. 4d–f).

AAV-gIR or AAV-gScrambled was bilaterally injected into the ARC of DIO AgRP-Cas9 mice (Fig. 4g). One week later, mice received bilateral intra-ARC administration of chABC or vehicle to disassemble neurofibrosis within the ARC. Consistent with our previous findings, chABC treatment in AAV-gScrambled mice led to weight loss, reduced adiposity, decreased caloric intake, enhanced energy expenditure and improved glycaemic control (Fig. 4h,i and Extended Data Fig. 6l–o). Remarkably, these metabolic improvements were significantly attenuated in chABC-treated AAV-gIR mice (Fig. 4h,i and Extended Data Fig. 6l–o), highlighting the crucial role of functional insulin receptor signalling in AgRP neurons. These results suggest that neurofibrosis contributes to metabolic disease through impaired insulin signalling in AgRP neurons and that degradation of ARC neurofibrosis improves whole-body metabolism and glycaemic control, partly by reinstating insulin signalling within AgRP neurons.

Hypothalamic inflammation drives neurofibrosis

Inflammation is intimately associated with ECM remodelling both peripherally and centrally, with increased ECM component deposition at sites of inflammation²⁵. Hypothalamic inflammation is demonstrated to precede obesity, positioning it as a possible driver for neurofibrosis development.

We observed diet-induced hypothalamic inflammation in the mediobasal hypothalamus of DIO mice (Extended Data Fig. 7a) and explored its role in neurofibrosis by administering anti-inflammatory AAVs expressing both soluble TNFR1 α (sTNFR1 α) and soluble TGF β R (sTGF β R) in the ARC prior to DIO onset (Extended Data Fig. 7b). Expression of sTNFR1 α and sTGF β R was confirmed, and their effectiveness was evidenced by significant downregulation of *Tnfa*, *Tgfb*, *Ikkb* and *Nfkb* expression after eight weeks of HFHS feeding (Supplementary Fig. 5a). Inhibition of hypothalamic inflammatory factors led to notable changes in the gene expression of ECM-remodelling proteases and their inhibitors, along with a substantial decrease in WFA expression and CS-GAG abundances in the ARC of treated mice (Extended Data Fig. 7c–e and Supplementary Fig. 5a,b). These findings demonstrate the capacity of hypothalamic inflammation to drive ARC PNN remodelling. Attenuation of neurofibrosis by inhibiting inflammation significantly reduced key metabolic disease markers, including diminished body weight gain, reduced adiposity, lower food intake, increased satiety, higher energy expenditure, prevention of BAT whitening, improved glycaemic control and enhanced insulin sensitivity (Extended Data Fig. 7f–i and Supplementary Fig. 5c–i). Attenuating hypothalamic inflammation also improved ARC neuronal insulin responsiveness and reduced AgRP inhibition of the PVH (Supplementary Fig. 5j–m).

To investigate the causative role of inflammation in neurofibrosis, we induced hypothalamic inflammation in healthy mice by co-administering AAV vectors to increase TNF α and TGF β expression in the ARC of 10-week chow-fed mice. Increased *Tnfa* and *Tgfb* expression was confirmed after eight weeks (Extended Data Fig. 7j and Supplementary Fig. 6a). This inflammation drove ARC PNN remodelling,

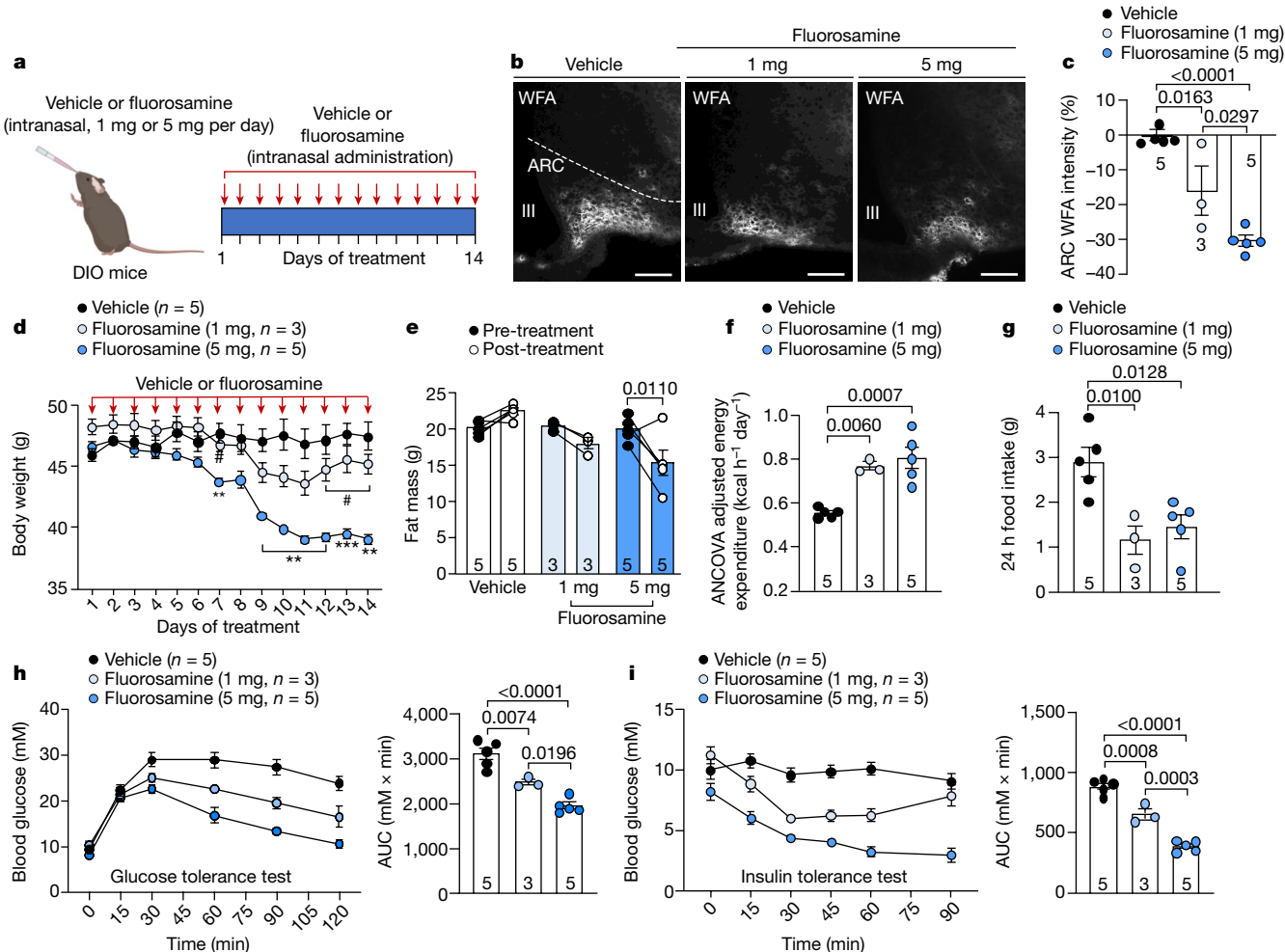


Fig. 5 | Intranasal delivery of neurofibrosis inhibitors promotes remission of metabolic disease. **a**, Twelve-week HFHS-fed male mice received daily intranasally delivered vehicle or fluorosamine (1 or 5 mg) for 14 days. **b–i**, WFA staining (**b**) and quantification (**c**), body weight (**d**), adiposity (**e**), energy expenditure (**f**), food intake (**g**), glucose tolerance (**h**) and insulin sensitivity (**i**)

of mice treated as in **a**. Data are mean ± s.e.m. Two-way ANOVA with multiple comparisons test (**d,e**) and one-way ANOVA with Tukey’s multiple comparisons (**c,f–i**). *P* values compare vehicle to 5 mg fluorosamine (*) or vehicle to 1 mg fluorosamine (#). *n* represents biologically independent samples; representative of at least two independent experiments. Scale bars, 100 μm.

evidenced by altered gene expression of ECM degrading proteases and their inhibitors, increased ARC PNN area and intensity, and higher CS-GAG abundances (Extended Data Fig. 7k–m and Supplementary Fig. 6a,b). Consistent with prior findings that hypothalamic inflammation drives whole-body metabolic dysfunction^{26–29}, we observed that inflammation-driven neurofibrosis within the ARC of lean mice led to weight gain, increased adiposity, hyperphagia, reduced satiety, lower energy expenditure, BAT whitening (indicated by gross morphology and histology), impaired glycaemic control, systemic insulin resistance and disrupted ARC metabolic neurocircuitry (Extended Data Fig. 7n–r and Supplementary Fig. 6c–l). Together, using both an anti-inflammatory and inflammatory approach, these results confirm that hypothalamic inflammation drives the remodelling of the ARC PNN, highlighting a novel aspect of the pathogenesis of hypothalamic inflammation.

These results identify the capacity of inflammation as a causal driver of ECM remodelling, yet the relative contribution of this remodelling in the manifestation of inflammation-driven hypothalamic dysfunction is unknown. To determine whether neurofibrosis is an essential pathophysiological mechanism by which inflammation drives metabolic disease, we combined pro-inflammatory AAVs with intra-ARC delivery of chABC (Extended Data Fig. 7j–l and Supplementary Fig. 6b). Critically, attenuation of inflammation-driven ECM remodelling reversed, at

least in part, the metabolic dysfunction observed following induction of hypothalamic inflammation (Extended Data Fig. 7n–r and Supplementary Fig. 6c–l). In summary, these results identify that hypothalamic inflammation promotes pathological PNN remodelling, which is a causal driver of whole-body metabolic dysfunction.

Inhibiting neurofibrosis promotes weight loss and improves glycemic control

Developing small-molecule inhibitors to reverse fibrotic ECM is a major therapeutic challenge. To explore the pharmacological potential for targeting neurofibrosis, we used fluorosamine (per-*O*-acetylated-4-*F*-*N*-acetylglucosamine), an enzyme inhibitor essential for CS-GAG chain assembly and elongation^{30,31}. Fluorosamine was delivered intracerebroventricularly (circumventing actions on peripheral tissues) to DIO mice for 10 days, leading to significant attenuation of neurofibrosis within the ARC but not in other brain areas such as the RSG and only partial attenuation in the habenula at the highest dose (Extended Data Fig. 8a–h). This effect may be due to the rapid turnover rate of the ARC PNN. Consistent with enzymatic PNN disassembly in the ARC, central fluorosamine treatment promoted weight loss, reduced adiposity, increased energy expenditure (independently of ambulatory activity), suppressed food intake through enhanced satiety, and improved

glycaemic control (Extended Data Figs. 8i–q and 9a–d). Mechanistically, fluorosamine improved glycaemic control by restoring ARC insulin sensitivity and enhancing whole-body insulin sensitivity, hepatic glucose production and tissue-specific glucose uptake in skeletal muscle, BAT and ingWAT, as shown by hyperinsulinaemic–euglycaemic clamps in weight-matched obese mice (Extended Data Fig. 9e–k). Fluorosamine also promoted remission of metabolic disease in late-stage type 2 diabetes (HFHS plus low dose streptozotocin; Extended Data Fig. 9l,m), highlighting that targeting neurofibrosis may be an effective method for treating various stages of type 2 diabetes progression.

Although fluorosamine and chABC differ in their mechanisms for disassembling the PNN, fluorosamine phenocopies the metabolic effects of chABC. To investigate whether the metabolic benefits of fluorosamine are mediated through insulin receptor signalling in AgRP neurons, we bilaterally injected AAV-gIR or AAV-gScrambled into the ARC of DIO AgRP-Cas9 mice, then treated them with vehicle or fluorosamine (100 µg intracerebroventricularly) daily for 10 days (Extended Data Fig. 9n). Recapitulating our earlier findings, fluorosamine treatment in AAV-gScrambled mice led to weight loss, reduced adiposity, decreased caloric intake, increased energy expenditure (independent of activity) and improved glycaemic control (Extended Data Fig. 9o–r and Supplementary Fig. 7a,b). However, these metabolic benefits were largely lost in AAV-IR mice, indicating that insulin receptor signalling in AgRP neurons is crucial for the metabolic effects of fluorosamine (Extended Data Fig. 9o–r).

To explore human therapeutic potential, we delivered neurofibrosis inhibitors intranasally in mice for targeted brain delivery. We assessed the biodistribution of biotin-conjugated fluorosamine delivered intranasally and found substantial accumulation, particularly within the ARC (Extended Data Fig. 10a,b). Intranasal fluorosamine administration to DIO mice for 14 days attenuated ARC neurofibrosis and achieved metabolic improvements similar to those observed with intracerebroventricular administration (Fig. 5a–i and Extended Data Fig. 10c–l). These findings introduce a first-in-class small-molecule inhibitor of neurofibrosis and establish the therapeutic capacity and utility of targeting neurofibrosis for the treatment of metabolic disease.

Discussion

The ECM is a dynamic structure that is essential for maintaining tissue function. Whereas controlled ECM remodelling is vital for organ health, dysregulated turnover–fibrosis–is a pathological feature of metabolic disease within peripheral tissues^{2,32}. Our study identifies pathological ECM remodelling in the ARC of the brain and highlights it as a key mechanism underlying the development of metabolic disease.

In obesity, AgRP neurons exhibit persistent excitability^{19,33}, driving hyperphagia and increased adiposity. The ECM of the brain—for example, PNN—can directly influence neuronal activity by binding to receptors, which enhances neurotransmitter and voltage-gated calcium activity²⁰. We have demonstrated here that pathological remodelling of the ARC PNN around AgRP neurons alters their intrinsic electrophysiological properties, promoting hyperactivity. Attenuating ARC neurofibrosis restores AgRP neuron function, reduces their inhibitory tone to the PVH, and improves hunger regulation, satiety, energy expenditure and glycaemic control.

The pathogenic effects of fibrosis in the peripheral tissues are well established, with increased fibrosis correlating with greater insulin resistance in both humans and mice^{2,34,35}. We have shown that neurofibrosis in the obese ARC has a causative role in neuronal insulin resistance by impeding insulin penetrance into the ARC. This reduced insulin sensitivity is linked to increased insulin binding to the negatively charged sulfated GAGs of the CSPGs that comprise the PNN³⁶. Additionally, the PNN may also promote insulin resistance at the receptor and intracellular levels³⁷. The ECM is crucial for cellular activity, and influences intracellular signalling pathways by interacting with cell

surface receptors^{38,39}. ECM components can activate integrin heterodimers, leading to the recruitment, assembly and phosphorylation of intracellular signalling complexes^{38–40}, and have been implicated in insulin resistance development in skeletal muscle, adipose tissues and liver^{10,41,42}. Thus, ARC PNN components likely also have a role in regulating intracellular signalling of metabolic hormones such as insulin.

Chronic inflammation in peripheral organs such as adipose tissue and the liver is marked by recruitment of immune cells and release of pro-inflammatory cytokines, which promotes fibrosis^{43–46}. Although hypothalamic inflammation drives metabolic imbalance in response to overnutrition^{27,28}, the role of inflammation-mediated ECM remodelling in the brain during obesity is unknown. Here we reveal a novel mechanism by which inflammation drives fibrotic remodelling of the ARC PNN, identifying this as a key factor in inflammation-driven hypothalamic dysfunction.

Targeting the ECM surrounding metabolic neurocircuitry rather than the neurocircuitry itself presents a significant therapeutic opportunity for metabolic disease. Our study underscores the importance of neurofibrosis as a disease target and validates its relevance by demonstrating that fluorosamine^{30,31}, a small-molecule inhibitor, effectively treats obesity and diabetes in pre-clinical models by targeting PNN deposition in the brain. These findings introduce a small-molecule inhibitor of neurofibrosis and establish the therapeutic capacity and utility of targeting neurofibrosis for the treatment of metabolic disease.

Online content

Any methods, additional references, Nature Portfolio reporting summaries, source data, extended data, supplementary information, acknowledgements, peer review information; details of author contributions and competing interests; and statements of data and code availability are available at <https://doi.org/10.1038/s41586-024-07922-y>.

1. Beddows, C. A. & Dodd, G. T. Insulin on the brain: the role of central insulin signalling in energy and glucose homeostasis. *J. Neuroendocrinol.* **33**, e12947 (2021).
2. Guglielmi, V. et al. Omental adipose tissue fibrosis and insulin resistance in severe obesity. *Nutr. Diabetes* **5**, e175 (2015).
3. Dodd, G. T. et al. A hypothalamic phosphatase switch coordinates energy expenditure with feeding. *Cell Metab.* **26**, 375–393.e377 (2017).
4. Dodd, G. T., Lee-Young, R. S., Bruning, J. C. & Tiganis, T. TCTP regulates insulin signaling in AgRP neurons to coordinate glucose metabolism with feeding. *Diabetes* **67**, 1246–1257 (2018).
5. Heni, M. et al. Central insulin administration improves whole-body insulin sensitivity via hypothalamus and parasympathetic outputs in men. *Diabetes* **63**, 4083–4088 (2014).
6. Kullmann, S. et al. Brain insulin sensitivity is linked to adiposity and body fat distribution. *Nat. Commun.* **11**, 1841 (2020).
7. Dodd, G. T. et al. Insulin regulates POMC neuronal plasticity to control glucose metabolism. *eLife* **7**, e38704 (2018).
8. Dodd, G. T. et al. Leptin and insulin act on POMC neurons to promote the browning of white fat. *Cell* **160**, 88–104 (2015).
9. Berria, R. et al. Increased collagen content in insulin-resistant skeletal muscle. *Am. J. Physiol. Endocrinol. Metab.* **290**, E560–E565 (2006).
10. Kang, L. et al. Diet-induced muscle insulin resistance is associated with extracellular matrix remodeling and interaction with integrin $\alpha 2\beta 1$ in mice. *Diabetes* **60**, 416–426 (2011).
11. Shijo, T. et al. Aberrant astrocytic expression of chondroitin sulfate proteoglycan receptors in a rat model of amyotrophic lateral sclerosis. *J. Neurosci. Res.* **96**, 222–233 (2018).
12. Mirzadeh, Z. et al. Perineuronal net formation during the critical period for neuronal maturation in the hypothalamic arcuate nucleus. *Nat. Metab.* **1**, 212–221 (2019).
13. Lupori, L. et al. A comprehensive atlas of perineuronal net distribution and colocalization with parvalbumin in the adult mouse brain. *Cell Rep.* **42**, 112788 (2023).
14. Sun, J. et al. Microglia shape AgRP neuron postnatal development via regulating perineuronal net plasticity. *Mol. Psychiatry* **29**, 306–316 (2023).
15. Kohnke, S. et al. Nutritional regulation of oligodendrocyte differentiation regulates perineuronal net remodeling in the median eminence. *Cell Rep.* **36**, 109362 (2021).
16. Fawcett, J. W., Oohashi, T. & Pizzorusso, T. The roles of perineuronal nets and the perinodal extracellular matrix in neuronal function. *Nat. Rev. Neurosci.* **20**, 451–465 (2019).
17. Margolis, R. U. & Margolis, R. K. Sulfate turnover in mucopolysaccharides and glycoproteins of brain. *Biochim. Biophys. Acta* **264**, 426–431 (1972).
18. Harrison, L. et al. Fluorescent blood–brain barrier tracing shows intact leptin transport in obese mice. *Int. J. Obes.* **43**, 1305–1318 (2019).
19. Bayer, S. B. et al. Leptin modulates the intrinsic excitability of AgRP/NPY neurons in the arcuate nucleus of the hypothalamus. *J. Neurosci.* **34**, 5486–5496 (2014).

20. Balmer, T. S. Perineuronal nets enhance the excitability of fast-spiking neurons. *eNeuro* **3**, ENEURO.0112-16.2016 (2016).
21. Stincic, T. L. et al. CRISPR knockdown of *Kcnq3* attenuates the M-current and increases excitability of NPY/AgRP neurons to alter energy balance. *Mol. Metab.* **49**, 101218 (2021).
22. Qiu, J. et al. Insulin excites anorexigenic proopiomelanocortin neurons via activation of canonical transient receptor potential channels. *Cell Metab.* **19**, 682–693 (2014).
23. Li, M. M. et al. The paraventricular hypothalamus regulates satiety and prevents obesity via two genetically distinct circuits. *Neuron* **102**, 653–667.e656 (2019).
24. Atasoy, D., Betley, J. N., Su, H. H. & Sternson, S. M. Deconstruction of a neural circuit for hunger. *Nature* **488**, 172–177 (2012).
25. Jahan, N. & Hannila, S. S. Transforming growth factor beta-induced expression of chondroitin sulfate proteoglycans is mediated through non-Smad signaling pathways. *Exp. Neurol.* **263**, 372–384 (2015).
26. Mendes, N. F. et al. TGF- β 1 down-regulation in the mediobasal hypothalamus attenuates hypothalamic inflammation and protects against diet-induced obesity. *Metabolism* **85**, 171–182 (2018).
27. Zhang, X. et al. Hypothalamic IKK β /NF- κ B and ER stress link overnutrition to energy imbalance and obesity. *Cell* **135**, 61–73 (2008).
28. Arruda, A. P. et al. Low-grade hypothalamic inflammation leads to defective thermogenesis, insulin resistance, and impaired insulin secretion. *Endocrinology* **152**, 1314–1326 (2011).
29. Clemenzi, M. N., Wellhauser, L., Aljghami, M. E. & Belsham, D. D. Tumour necrosis factor α induces neuroinflammation and insulin resistance in immortalised hypothalamic neurones through independent pathways. *J. Neuroendocrinol.* **31**, e12678 (2019).
30. Keough, M. B. et al. An inhibitor of chondroitin sulfate proteoglycan synthesis promotes central nervous system remyelination. *Nat. Commun.* **7**, 11312 (2016).
31. Stephenson, E. L. et al. Targeting the chondroitin sulfate proteoglycans: evaluating fluorinated glucosamines and xylosides in screens pertinent to multiple sclerosis. *ACS Cent. Sci.* **5**, 1223–1234 (2019).
32. Li, Q., Hata, A., Kosugi, C., Kataoka, N. & Funaki, M. The density of extracellular matrix proteins regulates inflammation and insulin signaling in adipocytes. *FEBS Lett.* **584**, 4145–4150 (2010).
33. Beutler, L. R. et al. Obesity causes selective and long-lasting desensitization of AgRP neurons to dietary fat. *eLife* **9**, e55909 (2020).
34. Ruggiero, A. D. et al. Skeletal muscle extracellular matrix remodeling with worsening glycemic control in nonhuman primates. *Am. J. Physiol.* **320**, R226–R235 (2021).
35. Jaskiewicz, K., Rzepko, R. & Sledzinski, Z. Fibrogenesis in fatty liver associated with obesity and diabetes mellitus type 2. *Dig. Dis. Sci.* **53**, 785–788 (2008).
36. Djerbal, L., Lortat-Jacob, H. & Kwok, J. Chondroitin sulfates and their binding molecules in the central nervous system. *Glycoconj. J.* **34**, 363–376 (2017).
37. Shulman, G. I. Cellular mechanisms of insulin resistance. *J. Clin. Invest.* **106**, 171–176 (2000).
38. Boura-Halfon, S., Voliovitich, H., Feinstein, R., Paz, K. & Zick, Y. Extracellular matrix proteins modulate endocytosis of the insulin receptor. *J. Biol. Chem.* **278**, 16397–16404 (2003).
39. Troussard, A. A. et al. Conditional knock-out of integrin-linked kinase demonstrates an essential role in protein kinase B/Akt activation. *J. Biol. Chem.* **278**, 22374–22378 (2003).
40. Singh, J. P. et al. The catalytic activity of TCPTP is auto-regulated by its intrinsically disordered tail and activated by Integrin α -1. *Nat. Commun.* **13**, 94 (2022).
41. Kang, L. et al. Integrin-linked kinase in muscle is necessary for the development of insulin resistance in diet-induced obese mice. *Diabetes* **65**, 1590–1600 (2016).
42. Williams, A. S. et al. Integrin-linked kinase is necessary for the development of diet-induced hepatic insulin resistance. *Diabetes* **66**, 325–334 (2017).
43. Lee, Y. S. et al. Inflammation is necessary for long-term but not short-term high-fat diet-induced insulin resistance. *Diabetes* **60**, 2474–2483 (2011).
44. Hardy, O. T. et al. Body mass index-independent inflammation in omental adipose tissue associated with insulin resistance in morbid obesity. *Surg. Obes. Relat. Dis.* **7**, 60–67 (2011).
45. Chakravarthy, A., Khan, L., Bensler, N. P., Bose, P. & De Carvalho, D. D. TGF- β -associated extracellular matrix genes link cancer-associated fibroblasts to immune evasion and immunotherapy failure. *Nat. Commun.* **9**, 4692 (2018).
46. Proudfoot, A. E. et al. Glycosaminoglycan binding and oligomerization are essential for the in vivo activity of certain chemokines. *Proc. Natl Acad. Sci. USA* **100**, 1885–1890 (2003).

Publisher's note Springer Nature remains neutral with regard to jurisdictional claims in published maps and institutional affiliations.



Open Access This article is licensed under a Creative Commons Attribution-NonCommercial-NoDerivatives 4.0 International License, which permits any non-commercial use, sharing, distribution and reproduction in any medium or format, as long as you give appropriate credit to the original author(s) and the source, provide a link to the Creative Commons licence, and indicate if you modified the licensed material. You do not have permission under this licence to share adapted material derived from this article or parts of it. The images or other third party material in this article are included in the article's Creative Commons licence, unless indicated otherwise in a credit line to the material. If material is not included in the article's Creative Commons licence and your intended use is not permitted by statutory regulation or exceeds the permitted use, you will need to obtain permission directly from the copyright holder. To view a copy of this licence, visit <http://creativecommons.org/licenses/by-nc-nd/4.0/>.

© The Author(s) 2024

Methods

Animals

Experiments were performed in accordance with ethics guidelines approved by The University of Melbourne, Monash University and St Vincents Research Institutes Animal Ethics Committee (10323, 10324, 10352, 10385, 10427, 21712, 22282, 22404, 25349 and 28097). Mice were maintained on a 12 h light-dark cycle in a temperature-controlled high-barrier facility with free access to food and water per NHMRC Australian Code of Practice for the Care and Use of Animals. C57BL/6j mice were sourced from the Animal Resources Centre, Australia, whereas *Agrp*-IRES-Cre (strain 012899), *db/db* (strain 000697), *Npy*-GFP (strain 006417), *Pomc*-GFP (strain 009593), LSL-Cas9 (strain 028551), NZO (strain 002105) mice were sourced from Jackson Laboratories. To generate *Agrp*-IRES-Cre;LSL-Cas9-GFP (AgRP-Cas9) mice, hemizygous *Agrp*-IRES-Cre mice were bred with homozygous LSL-Cas9-GFP mice. All experimental interventions were performed in male rodents aged 8–10 weeks old, unless stated otherwise. Male Sprague–Dawley rats (Animal Resources Centre, Australia) were housed individually with nesting and enrichment material at a room temperature of 23 ± 2 °C, room humidity 40–70%, on a reverse 12 h light/dark cycle (lights off at 09:00). Animals were fed a standard chow (Barastoc, Ridley AgriProducts), a high-fat high-sugar diet (mice: 43% and 20% of total energy from fat and carbohydrate respectively, SF04-001, Specialty Feeds; rats: 30% fats of total energy SF17-204, Specialty Feeds) or a high-fat high-cholesterol diet (40% of total energy from fat and 2% cholesterol, SF16-033, Specialty Feeds). To induce late-stage type 2 diabetes in mice, male C57BL/6j mice were fed a HFHS diet for 4 weeks before being receiving up to 6 intraperitoneal injections of streptozotocin (40 mg kg^{-1} (Sigma) in 50 mM sodium citrate buffer pH 4.5) over the following 2 weeks. Blood glucose levels were monitored and mice exhibiting stable blood glucose levels of $>15 \text{ mM}$ were used for downstream experiments. For all experiments, random allocation was used for assignment of individual mice to experimental groups, and sample sizes were chosen on the basis of prior work and according to standards in the field.

Genotyping

DNA was extracted from tail biopsies using Tissue Extract-PCR Buffers (MDX004, Meridian Bioscience) and DNA was amplified by PCR using MyTaq HS Red Mix (BIO-25048, Meridian Bioscience) with the following primers to detect *cre* (forward: 5'-GCGGTCTGGCAGTAAAACTATC-3', reverse: 5'-GTGAAACAGCATTGCTGTCACCT-3'), LSL-Cas9 (wt forward: 5'-AAGGGAGCTGCAGTGGAGTA-3', wt reverse: 5'-mCAGGACAACGCCACACA-3', mt forward: 5'-TCCCATCAAGCTGATCC-3', mt reverse: 5'-CTTCTCTTTGGGGCCATCT-3'), *Npy*-GFP (common forward: 5'-TATGTGGACGGGCGAGAAGATCCAGG-3', wt reverse: 5'-CCAGCTCACATATTTATCTAGAG-3', mt reverse: 5'-GGTGGCGGTGCGCTACTGGA-3'), *Pomc*-GFP (forward 5'-AAGTTCATCTGCACCACCG-3', reverse 5'-TGCTCAGGTAGTGGTTGTCG-3') alleles. The following primers were used to monitor the CRISPR-mediated deletion of the mouse insulin receptor gene ($\Delta Ins^{\text{CRISPR}}$): forward 5'-GAGATGGTCCACCTGAAGGA-3', reverse 5'-GTGAAGGTCTTGGCAGAAGC-3'.

Immunohistochemistry

For immunohistochemistry on brain, mice were anaesthetized and perfused transcardially with heparinized saline ($10,000 \text{ units l}^{-1}$ porcine heparin) followed by 10% neutral buffered formalin. Brains were post-fixed for 16 h and kept for three days at 4 °C in 30% sucrose in PBS to cryoprotect the tissue, before freezing on dry ice. Thirty-micrometre sections (120 mm apart) were cut in the coronal plane throughout the entire rostral–caudal extent of the hypothalamus. Sections were stored in cryoprotectant (30% ethylene glycol, 20% glycerol in PBS) at -20 °C for long term storage. For the detection of hyaluronic acid and versican

only, sections were subjected to heat-induced epitope retrieval using citrate acid buffer (10 mM sodium citrate, 0.05% Tween 20, pH 6.0) at 95 °C for 20 min.

For detection of aggrecan, GFP, hyaluronic acid, mCherry, versican, tenascin C, HAPLN1, neurocan, phosphacan, brevican, WFA, WFA-FITC, PGP9.5 and AgRP, sections were incubated at room temperature for 1 h in blocking buffer (0.3% Triton X-100, 5% normal goat serum, Gibco, Thermo Fisher, 0.02% sodium azide) and then overnight at 4 °C in 1% blocking buffer containing either rabbit anti-aggrecan (1:1,000, AB1031, Millipore), chicken anti-GFP (1:2,000; ab13970, Abcam), biotinylated hyaluronic acid binding protein (1:100, 385911, Millipore), rabbit anti-dsRed (1:2,000, 600-401-379, Rockland), rabbit anti-versican (1:1,000, AB1033, Millipore), tenascin C (1:500, MI-B4, Developmental Studies Hybridoma Bank), HAPLN1 (1:500, 9/30/8-A-4, Developmental Studies Hybridoma Bank), neurocan (1:300, 1F6-S, Developmental Studies Hybridoma Bank), phosphacan (1:300, 3F8, Developmental Studies Hybridoma Bank), brevican (1:500, 610895, BD Transduction Laboratories), biotinylated WFA (1:2,000, L1516; Sigma-Aldrich), WFA-FITC (1:2,000, FL-1351-2, Vector Laboratories), rabbit anti PGP9.5 (1:1,000, 14730-1-AP, Proteintech), or guinea pig anti-AgRP (1:500, AS506, Antibodies Australia). After washing with PBS-T (0.3% Triton X-100 in PBS + 0.02% sodium azide), sections were incubated with goat anti-chicken–Alexa Fluor 488 (ab150169, Abcam), goat anti-rabbit–Alexa Fluor 488, goat anti-rabbit–Alexa Fluor 595 or goat anti-rabbit–Alexa Fluor 647 (ab150077, ab150080 or ab150083, respectively, Abcam), Streptavidin–Alexa Fluor 594 or Streptavidin–Alexa Fluor 647 Streptavidin (405240, BioLegend) in 5% blocking buffer for 2 h at room temperature. Sections were mounted with Mowiol 4–88 mounting media and visualized with an Olympus BX61 microscope. Images were captured with an Olympus BX61 camera, acquired using Olympus cellSens Dimension software v2.1 and processed using ImageJ software v1.53 s (NIH). Images for cell internalization were captured using a Zeiss LSM880 Airyscan Fast confocal microscope, acquired using Zeiss ZEN software v2.1 and processed using ImageJ v1.53 s (NIH). Brightness and contrast have been adjusted to aid in the analysis and visualization.

For ingWAT, eWAT, liver and BAT immunohistochemistry, tissue was immediately dissected and fixed in buffered formalin solution on a rocking platform for 48 h at room temperature. Tissues were embedded in paraffin, and 5- μm sections $100 \mu\text{m}$ apart were prepared. For haematoxylin and eosin histology, sections were incubated in haematoxylin for 3 min followed by 30 s in eosin. For detection of UCPI, ingWAT sections were subjected to antigen retrieval in citrate acid buffer (10 mM sodium citrate, 0.05% Tween 20, pH 6.0) at 95 °C for 20 min. Sections were incubated at room temperature for 1 h in 5% blocking buffer and then overnight at 4 °C in rabbit anti-UCPI (1:1,000; ab10983, Abcam), in 1% blocking buffer. Following washing in PBS-T, sections were incubated with goat anti-rabbit Alexa Fluor 488 (ab150077, Abcam) secondary antibody in 5% blocking buffer for 2 h at room temperature. Sections were incubated in DAPI (20 ng ml^{-1} in PBS) for 10 min then mounted with Mowiol 4–88 mounting media and visualized with an Olympus BX61 microscope. Images were captured with an Olympus BX61 camera, acquired using Olympus cellSens Dimension software v2.1 and processed using ImageJ software v1.53 s (NIH). Brightness and contrast have been adjusted to aid in the analysis and visualization.

Functional p-AKT and p-STAT3 Immunohistochemistry

Mice were injected intraperitoneally with vehicle (PBS) or insulin (3 mU g^{-1} , Actrapid, Nova Nordisk) and mice were transcardially perfused (as described above) after 15 min with 10% neutral buffered formalin. For p-STAT3 signalling, mice were intravenously injected with vehicle (PBS) or leptin ($20 \mu\text{g}$ per mouse in a volume of $100 \mu\text{l}$) and transcardially perfused after 30 min with 10% neutral buffered formalin. The brains were post-fixed for 16 h on a rocking platform at room temperature and then kept for two days in 30% sucrose in PBS

Article

to cryoprotect the tissue, before freezing on dry ice. 30 μm sections were cut in the coronal plane throughout the entire rostral–caudal extent of the hypothalamus. Sections were pre-treated for 20 min in freshly prepared 1% NaOH, 1% H_2O_2 in PBS, washed in PBS, incubated for 10 min in 0.3% glycine, washed in PBS and incubated for 10 min in 0.03% SDS. Sections were then blocked in 5% blocking buffer for 1 h at room temperature and incubated for 48 h with rabbit anti-p-AKT (Ser473) (1:300; 4060, Cell Signaling Technology), rabbit anti p-STAT3 (Tyr705) (1:500, number 9131S, Cell Signaling Technology), or rabbit anti fluor in 1% blocking buffer. Sections were then incubated in 5% blocking buffer containing either goat anti-rabbit Alexa Fluor 647 (ab150083, Abcam), goat anti-rabbit Alexa Fluor 594 (ab150080, Abcam) or biotinylated goat anti-rabbit (BA-1000, Vector Laboratories, no sodium azide in 5% blocking buffer). Fluorescence sections were mounted with Mowiol 4–88 mounting media and visualized using Olympus BX61 microscope. Images were captured with an Olympus BX61 camera, acquired using Olympus cellSens Dimension software v2.1 and processed using ImageJ software v1.53 s (NIH). For chromogenic detection, p-AKT signal was amplified using Vectastain ABC-HRP Kit (1:500, PK-4000, Vector Laboratories) and visualized using 0.1% H_2O_2 DAB solution (3,30-diaminobenzidine, ICN980681, Thermo Fisher) Peroxidase Substrate Kits (Vector Laboratories). p-STAT3 and p-AKT immunopositive cells were visualized with a Leica DM2000 LED bright field microscope using a Leica DMC6200 camera and Leica Application Suite X software. Brightness and contrast have been adjusted to aid in the analysis and visualization.

PNN immunofluorescent analysis

The ARC PNN was stereologically assessed throughout the entire rostro-caudal ARC. The ARC was divided into three regions, including the rostral ARC (–1.22/–1.58 mm anterior–posterior), medial ARC (–1.58/–1.94 mm anterior–posterior) and caudal ARC (–1.94/–2.18 mm anterior–posterior). PNN was quantified in the VMH and RSG cortex (–1.58/–1.94 mm anterior–posterior).

All image quantification was performed in ImageJ v1.53 s (NIH). Raw images underwent background subtraction using a rolling ball algorithm to minimize background and any potential variance in tissue autofluorescence. To quantify area and intensity of the PNN within each brain region (ARC, VMH or RSG cortex) images were thresholded and binarized to create a region of interest (ROI) mask of only the PNN. For each brain area, PNN ROI area (μm^2) and intensity was calculated. This process was automated to minimize bias and to account for differences in brain nuclei size across multiple images. Brain nuclei were defined in accordance with the Paxinos and Franklin Mouse Brain Atlas (<http://labs.gaidi.ca/mouse-brain-atlas/>). The area and intensity of PNN within each region was normalized to the respective control.

To determine the co-localization of ECM components (hyaluronic acid, HAPLN1, tenascin C, aggrecan, versican, phosphacan, brevican, neurocan) within the PNN (WFA-positive staining), 2 masks were generated per image: one for the total PNN staining and another for component staining within the ARC. The overall area and intensity were calculated for the total PNN structure. The area and intensity for components within the PNN was determined by quantifying the expression within the total PNN mask only. This allowed for the characterization of ECM components expressed specifically within the ARC PNN. The area and intensity of PNN within each region was normalized to the respective control. To determine the co-localization of the WFA-labelled ARC PNN within the ARC PNN components, two masks were generated per image: one for total PNN staining and another for component staining within the ARC. The overall area and intensity were calculated for the total component structure. The area and intensity for the PNN comprising the components was determined by quantifying the WFA expression within the total component mask only. The area and intensity of PNN within each region was normalized to the respective control. This combined approach further characterizes the specificity of the

components to the PNN region. Brightness and contrast have been adjusted to aid in the analysis and visualization.

Quantification of ARC neurons within the PNN

To determine which metabolically relevant ARC neurons are encased within the PNN during the development of metabolic disease we analysed brains taken from 0, 4- and 12-week HFHS-fed *Npy*-GFP (to visualize AgRP/NPY neurons) and *Pomc*-GFP (to visualize POMC neurons) mice. ARC sections were stained for GFP and WFA as described in 'Immunohistochemistry' and analysed using ImageJ v1.53 s (NIH) software. To determine the number of GFP positive neurons encased within the PNN we generated two masks. To define the PNN structure in the ARC, images were thresholded and binarized to create a PNN mask. To identify individual GFP positive neurons, images were thresholded and binarized to create a GFP mask. To define individual GFP neurons, the GFP masks were segmented using a watershed separation algorithm. The total number of GFP positive cells were counted within the whole ARC area and within the PNN mask. This quantified the percent of GFP cells encompassed by the PNN in the ARC.

To determine the intensity of the PNN that specifically surrounds individual GFP cells in the ARC, GFP images were thresholded and binarized. An ROI of 1.29 μm (average size of ECM surrounding cortical neurons⁴⁷) was generated around each GFP cell using dilate, distance map and Voronoi processes in ImageJ v1.53 s software. This generated a mask capable of specifically analysing PNN bordering individual GFP cells. Using this mask, PNN staining intensity surrounding GFP cells present within the ARC PNN was determined.

Behavioural satiety sequence

Mice were fasted overnight and housed individually in transparent cages with ad libitum access to water. Two hours after the beginning of the light cycle (at 09:00) pre-weighed food was presented to the mice and mice were undisturbed and discreetly observed for 90 min. Momentary behaviour was scored every 30 s over a 90-min observation. Behaviour at each 30 s interval was recorded according to the following classifications: feeding (animal at hopper trying to obtain food, chewing, or gnawing), drinking (animal licking at the water spout), grooming (animal scratching, biting or licking any part of its anatomy), resting (animal curled up, resting head with eyes closed), active (animal showing activity, including locomotion, sniffing, rearing), or inactive (animal immobile when aware, or signs of sickness behaviour). Data were collated into 5-min bins, and several variables were assessed including the average percentage of time the mice spent engaging in each recorded behaviour (percentage of total behaviour), food intake, the transition from eating to resting and the time to satiety (the time when the frequency of eating behaviour intersects with the frequency of resting behaviour).

Stereotaxic surgery

All stereotaxic injections were undertaken under isoflurane anaesthetic using an Ultra Precise Stereotaxic Instrument (963 Kopf) or Ultra Precise Rotational Stereotaxic Instrument (69100, RWD Life Sciences) alongside stereotaxic nanoinjectors (788130, KD Scientific) with Neurosyringes (Hamilton). To induce hypothalamic inflammation, mice were bilaterally injected with a 1:1:1 cocktail containing AAVs expressing GFP (AAV-CMV-eGFP, Addgene) and ligands for TNF (AAV-CMV-TNF) and TGF β (AAV-CMV-TGF β) or control AAV alone (AAV-CMV-eGFP, Addgene). To inhibit hypothalamic inflammation mice received bilateral injections of a 1:1:1 AAV cocktail containing expressing soluble TNF Receptor Superfamily 1A (AAV-CMV-sTNFR1A), soluble TGF β R2 (AAV-TRE-sTGF β R2 and AAV-CMV-TetOFF) and AAV-CMV-eGFP vector, or control AAV alone (AAV-CMV-eGFP, Addgene). All inflammatory AAVs were delivered at $\sim 10^{12}$ GU ml^{-1} . To disassemble the PNN within the ARC, mice received bilateral (unless stated otherwise) administration of 15 mU per side of active chABC (C3667, Sigma; dissolved in 1 M

trehalose) or heat-inactivated chABC protein as a vehicle (chABC in 1 M trehalose⁴⁸ was heat-inactivated at 85 °C for 45 min, as previously described⁴⁹) in a total volume of 150 nl per side. To pulse the PNN within the ARC or RSG, mice received bilateral (unless stated otherwise) administration of biotinylated WFA (0.3 µg per side, in a volume of 150 nl). To disrupt the insulin receptor in AgRP neurons, 12-week HFHS-fed AgRP-Cas9 mice were stereotaxically injected with AAV vectors expressing U6-driven guide RNA's targeting the *Insr* gene or a scrambled sequence (5'-GTGTAGTTCGACCATTCGTG-3') alongside a CAG driven mCherry FLEX switch. Unless otherwise stated injections were delivered bilaterally into the ARC (coordinates, bregma: anterior-posterior, -1.70 mm; dorsal-ventral, -5.85 mm; lateral, ±0.18 mm, 200 nl per side) or into the RSG (coordinates, bregma: anterior-posterior, -1.70 mm; dorsal-ventral, -1.00 mm; lateral, ±0.20 mm, 200 nl per side). WFA-biotin was injected unilaterally into the cc (coordinates, bregma: anterior-posterior, -1.70 mm; dorsal-ventral, -1.50 mm; lateral, ±0.20 mm, 200 nl per side).

Hyperinsulinaemic-euglycaemic clamps in conscious freely behaving mice

For hyperinsulinaemic-euglycaemic clamps, mice were anaesthetized under isoflurane and the right jugular vein was catheterized for infusions, as previously described⁴. Catheters were attached to an implant button (BMSW25, RWD Life Sciences). Implant buttons were capped allowing for group mousing of mice and catheters were kept patent by flushing daily with 40 µl heparinized saline. On the day of the experiment, food was removed at 07:00. After 3.5 h fasting, a primed (1 min, 1.25 µCi min⁻¹) continuous infusion (0.05 µCi min⁻¹) of [3-³H] glucose (NET331A001MC, PerkinElmer) was administered to measure whole-body glucose turnover, as described⁴. Ninety minutes later, mice received a 40 mU kg⁻¹ insulin bolus over 10 min which was followed by continuous insulin infusion (4 mU kg⁻¹ min⁻¹ in gelofusine). Euglycaemia (-8-10 mM blood glucose) was maintained by a variable infusion of a 30% glucose solution.

Tail blood samples were collected during steady-state conditions (rate of appearance (Ra) = rate of disappearance (Rd)) and at 80, 90, 100, 110, and 120 min for determination of Rd and Ra, as described above. At 120 min, a 13 µCi bolus of [¹⁴C]-2-deoxy-D-glucose (NEC495A250UC, PerkinElmer) was injected into the jugular vein, and blood was sampled at 122, 125, 135, 145 and 155 min. At the end of the experiment tissues were extracted for glucose uptake determinations.

Pair feeding

HFHS-fed C57BL/6J mice were bilaterally injected with vehicle or chABC into the ARC. 24 h food intake was determined for intra-ARC chABC-treated mice and a cohort of intra-ARC treated vehicle-treated mice were pair-fed, whereby food availability was restricted to the average food consumed by intra-ARC chABC-treated mice.

Metabolic assessment

Metabolic measurements were undertaken in the Melbourne Mouse Metabolic Phenotyping Platform (The University of Melbourne, Australia). Glucose tolerance tests were performed on 6 h fasted conscious mice respectively by injecting D-glucose (2 mg per g of lean body mass and 1 mg per g lean mass for *db/db* and HFHS + streptozotocin mice) into the peritoneal cavity and measuring glucose in tail blood immediately before and at 0, 15, 30, 45, 60, 90 and 120 min after injection using an Accu-Check glucometer (Roche). The areas under glucose excursion curves were determined and expressed as mM × min. Fasted (12 h fast) plasma insulin or glucose levels were determined using a Rat/Mouse Insulin ELISA (EZRMI-13K, Merck Millipore) or an Accu-Check glucometer respectively. The HOMA-IR was calculated using the equation [(glucose × insulin)/405]. Adiposity was measured using TD-NMR minispec with OPUS 7.0 spectroscopy software (Bruker Optics).

Mice were acclimated for 24 h and then monitored for 48 h in an environmentally controlled Promethion Metabolic Screening System (Sable Systems International) fitted with indirect open circuit calorimetry, food consumption and activity monitors to measure activity, caloric intake and energy expenditure. Data were recorded and extracted using MetaScreen v2.3.15.13 and Macro Interpreter v23.6.0 (Sable Systems International). Respiratory quotients were calculated as the ratio of CO₂ production over O₂ consumption respiratory exchange ratio and energy expenditure was calculated using the Weir equation (energy expenditure (kcal h⁻¹) = 60 × (0.003941 × VO₂ + 0.001106 × VCO₂). To account for difference in body mass/composition energy expenditure was analysed and adjusted using ANCOVA using scripts available at the National Mouse Metabolic Phenotyping Centers (MMPC) energy expenditure analysis page (<https://www.mmpc.org/shared/regression.aspx>).

To provide an index of ingWAT and BAT thermogenesis, infrared thermography was used to measure temperature changes in the inguinal and interscapular regions as described previously⁵⁰. The FLIR T1010 thermal imaging camera (FLIR Systems Australia) was mounted onto a tripod and animals were positioned at a standardized distance of 70 cm from the camera. Animals were anaesthetized, shaved in the regions of interest and whole-body images were collected in both the prone and supine positions. Temperatures were analysed using the FLIR ResearchIT Max 4 program (FLIR Systems). The peak temperatures within the ingWAT and BAT was determined.

Viral vector production

To generate the AAV-gScrambled (pAAV-U6>mScramble-GTGTAGTTCGACCATTCGTG)-CAG > LL:rev(mCherry):rev(LL):WPRE) and AAV-gIR (pAAV[-U6>mInsr[gRNA-TATCGACTGGTCCCGTATCC]-U6>mInsr[gRNA-GTCTGTCCAGGCACCGCAA]-CAG > LL:rev(mCherry):rev(LL):WPRE) viral vectors, sgRNAs were first designed using online CRISPR tools (<http://crispr.mit.edu> and <http://chopchop.cbu.uib.no/>). Potential off-target gRNA binding was assessed in silico using Off-Spotter (<https://cm.jefferson.edu/Off-Spotter/>) and guides exhibiting ≥3 mismatch with non-specific genomic regions were considered. For AAV-gScrambled a pUp-U6>Scrambled gRNA vector was generated using the Gibson assembly of a pDONR P4-P1R backbone and primers 5'-GGGGACAACCTTTGTATAGAAAAGTTGGAGG GCCTATTTCCCATGATTC-3' and 5'-GGGACTGCTTTTTTGTACAA ACTTGAAAAAAGCACCGACTCGGTGCC-3'. For AAV-gIR a pUp-U6>mInsr[gRNA-TATCGACTGGTCCCGTATCC]-U6>mInsr[gRNA-GTCTGTCCAGGCACCGCAA] gRNA vector was generated using the Gibson assembly of a AarI digested pUp-U6-gRNA-AarI-Stuffer-AarI backbone and primers 5'-ATATCTTGTGGAAAGGACGAAACACCGTATCGACTG TCCCGTATCCG-3' and 5'-AACTTGCTATTCTAGCTCTAAAACCTT GGCGGTGCCTGGACAGAC-3'. For both AAV-gScrambled and AAV-gIR the p-Up vectors were cloned alongside pDown-CAG and pTail-LL:rev(mCherry):rev(LL) to generate the final vectors by LR reaction using the Gateway method. The AAV plasmids were used to generate recombinant viral vectors packaged into the AAV-DJ/8 pseudotype supplied at a titre of >2 × 10¹³ GC ml⁻¹. All vector cloning and AAV packaging was carried out by VectorBuilder (Chicago, IL). The recombinant AAV vectors expressing inflammatory factors TNF (AAV-CMV-TNF) and TGFβ (AAV-CMV-TGFβ), or soluble TNF receptor superfamily 1A (AAV-CMV-sTNFRA1) or TGFβ receptor 2 (AAV-TRE-sTGFβR2 and AAV-CMV-TetOFF), were manufactured in-house as described previously⁵¹. In brief, cDNA constructs carrying the relevant gene expression cassettes flanked by AV2 terminal repeats in an AAV expression plasmid were transfected with the pDGM6 packaging plasmid into HEK293T cells (Sigma; authenticated by Sigma and not tested for mycoplasma contamination) by means of the calcium phosphate precipitate method to produce AAV6 vectors. At 72 h after transfection, the media and cells were harvested for purification via heparin affinity column (HiTrap, GE Healthcare) chromatography and overnight ultracentrifugation before

Article

re-suspension in sterile physiological Ringer's solution and titre determination via quantitative PCR-based reaction (Applied Biosystems) as described previously⁵². Purified vectors were stored frozen until the day of use, at which time they were rapidly thawed at room temperature and diluted in sterile PBS for administration via stereotaxic injection as described herein.

Insulin and leptin extravasation in the ARC

12-week HFHS-fed C57BL/6J or aged-matched chow-fed controls received bilateral injections of vehicle or chABC into the ARC. 3 days post-injection (before differences in body weights were seen), mice were fasted for 6 h. To assess insulin extravasation into the ARC mice were administered insulin-FITC (50 µg per mouse in a volume of 100 µl, intravenous injection, I3661, Sigma) or FITC (64.3 µmol per mouse in a volume of 100 µl, intravenous injection, F3651, Sigma). To assess leptin extravasation into the ARC, mice were administered leptin-647 (20 µg per mouse in a volume of 100 µl). Mice were perfused (as described above) 30 min post-injection. To assess insulin extravasation into the ARC irrespective of the BBB, mice were administered insulin-FITC (1 µg per mouse in a volume of 2 µl) directly into the lateral ventricles. To do this, mice were anaesthetized and stereotaxically injected (as described above) insulin-FITC at a rate of 200 nl min⁻¹ into the lateral ventricles (coordinates, bregma: anterior-posterior, -0.20 mm; dorsal-ventral, -2.4 mm; lateral, +0.10 mm). Mice were perfused (as described above) 20 min from the start of injection. To assess insulin-FITC brains were post-fixed overnight and cryoprotected in 30% sucrose in PBS. To retain spontaneous fluorescence signal, brains and sections were kept in the dark and were mounted and imaged immediately after sectioning.

Lateral ventricle cannulations

Under isoflurane anaesthetic 12-week HFHS-fed C57BL/6J or AgRP-Cas9 mice were implanted stereotaxically with guide cannulas into the right lateral ventricle (0.2 mm posterior, 1.0 mm lateral from bregma). Guide cannula was positioned 1.3 mm above the injection site (1 mm ventral to the surface of the skull). AgRP-Cas9 mice were treated with either AAV-gScrambled or AAV-gIR and underwent guide cannula placement 7 days post AAV administration. Mice were administered intracerebroventricular vehicle (ddH₂O), fluorosamine (100 µg per day or 250 µg per day) in a volume of 2 µl and all compounds were delivered approximately 1 h before lights off (19:00).

Intranasal drug delivery

Conscious mice were restrained by scruffing and inverted parallel to the floor with the chin at -180-degree angle with the neck. Using a 10 µl tip, a pipettor was loaded with 5 µl of vehicle (ddH₂O) or fluorosamine (1 mg per mouse in 20 µl or 5 mg per mouse in 20 µl). The tip of the filled pipettor was placed near the left nostril at a 45-degree angle, and the drug was ejected to form a small 5 µl droplet at tip for the mouse to inhale. Immediately after the mouse inhaled the first droplet the remaining solution was ejected to form another small droplet for the mouse to inhale through the same nostril. The mouse was held in this position for 15 s before the procedure was repeated in the right nostril. The mouse was returned to the cage for 2 min and the process was repeated so that each mouse received four droplets of 5 µl each, delivering a total of 20 µl of solution. All drugs were administered delivered approximately 1 h before lights off (19:00).

PNN tracker validation and quantification

To determine PNN turnover in the ARC, RSG, or CC, mice received stereotaxic injections of WFA-biotin as described in 'Stereotaxic surgery'. At experimental endpoints mice were transcardially perfused and assessment of pulse labelled ARC PNN was identified by immunofluorescent detection of WFA-biotin (PNN at the time of pulse) and WFA-FITC (total PNN) as described in 'Immunohistochemistry'.

To chase the pulsed WFA-biotin in the ARC, sections were imaged and analysed using ImageJ v1.53 s (NIH) software. Raw images underwent background subtraction using a rolling ball algorithm to minimize background and tissue autofluorescence. To quantify staining area within the ARC, images were thresholded and binarized to create ROI masks for WFA-biotin and WFA-FITC. For each image, staining ROI area (µm²) and intensity was calculated.

To validate the PNN tracker technique, C57BL/6J mice were stereotaxically injected unilaterally with WFA (0.3 µg per side, in a volume of 150 nl) to pulse the PNN into one side of the ARC and saline injected into the other side. One day later mice were transcardially perfused and ARC brain sections were stained and analysed for PNN tracker analysis. To determine how faithfully the pulsed WFA-biotin represents the current PNN we quantified the percentage area to which WFA-biotin (pulse labelled) co-localizes with WFA-FITC (total present PNN).

To validate that the chased WFA-biotin signal represents bona fide PNN staining we stereotaxically injected WFA (0.3 µg per side, in a volume of 150 nl) bilaterally into the ARC of 8-week-old C57BL/6J mice. 3 days later mice received unilateral ARC injections of chABC (15 mU per side in a volume of 150 nl) or vehicle to disassemble the WFA-biotin bound PNN. To determine the specificity of pulsed WFA-biotin we quantified and compared the area and intensity of WFA-biotin staining in the chABC and vehicle-treated sides of the ARC.

To determine PNN turnover in lean and obese mice, we stereotaxically injected WFA-biotin (0.3 µg per side, in a volume of 150 nl) bilaterally into the ARC of 12-week HFHS-fed C57BL/6J mice or aged-matched controls. Brains were extracted either the day after surgery (day 0) or following 1, 3, 5 and 10 weeks post-injection. Brain sections were stained for the presence of WFA-biotin and WFA-FITC, and we quantified the area of WFA-biotin staining as described above. To determine PNN turnover we compared WFA-labelled PNN present at the start of the experiment (day 0) to that which remained at weeks 1, 3, 5 and 10. WFA-FITC labelling of the PNN was performed at each time point to validate the presence of the ARC PNN and ensure changes in WFA-biotin labelling were not due to loss of the PNN over time. The same process was used to assess turnover in the RSG and blood vessels of the CC.

ARC CS-GAG and hyaluronic acid disaccharide quantification

Microdissected ARC tissues were incubated in the extraction buffer, containing 8 M urea, 0.5% Triton X-100, 5 mM Tris 2-carboxyethylphosphine and cOmplete mini EDTA-free protease inhibitor cocktail (Merck) for 30 min with gentle mixing and then homogenized. Samples were centrifuged for 30 min at 5,000 rpm and the supernatant was collected and buffer exchanged using Amicon Ultracell-10K MWCO centrifugal tubes into PBS. Protein concentration of each sample was estimated using Bradford assay. Thirty µg of each protein extract was reduced using 5 mM dithiothreitol for 30 min at 50 °C and alkylated with 10 mM iodoacetamide for an hour at room temperature before blotting onto 0.45 µm PVDF membrane (Millipore, IPVH20200) and dried. Each sample spot was transferred into a 96-well plate and blocked using 1% (v/v) polyvinylpyrrolidone solution in water.

The disaccharide analysis procedure was adapted from⁵³ with the following modifications. GAG disaccharides were released from the PVDF sample spots using an enzyme mix containing 5 mU chABC (Sigma, Cat# C3667), 50 ng each of heparinase I/II/III (R&D Systems) in 100 mM ammonium acetate pH 7 with 5 mM calcium chloride and incubated at 30 °C overnight. An additional mixture of purified GAG polysaccharides containing 1 µg each of bovine kidney heparan sulfate (Sigma-Aldrich, H7640), 10 µg shark chondroitin sulfate (Sigma-Aldrich, C4382) and 1 µg of *Streptococcus equi* hyaluronic acid (Sigma-Aldrich, 53747) were digested alongside samples as enzyme reaction controls, and as retention time standards. Digested disaccharides were collected and dried under low pressure for labelling using 2-AB (2-aminobenzamide), according to a commercially available protocol (Ludger LT-KAB-VP24-Guide-v2.0). Samples, alongside

a standard mix of 8 common HS (Iduron, HS mix) and 8 common chondroitin sulfate disaccharides (Iduron, chondroitin sulfate mix), were labelled with 2-AB and washed with octanal twice to remove excess labelling agent. Cleaned samples in the aqueous layer were dried and resuspended in 75% (v/v) acetonitrile with 10 mM ammonium acetate, pH 6.8.

The labelled disaccharides were separated by liquid chromatography using a SeQuant ZIC-HILIC column (200 Å pore size, 3.5 µm particle size, 1 mm × 150 mm) at 35 °C using an Agilent 1260 Infinity II with fluorescence detection. The mobile phase solvent A (10 mM NH₄Ac, pH 6.8) and solvent B (90% acetonitrile in 10 mM NH₄Ac pH 6.8) were run at a constant flow rate of 60 µl min⁻¹ in microflow mode with gradient parameters as follows: 0–3 min, 100% B; 4–14 min, 94% B; 34 min, 86% B; 47 min, 75% B; 51 min, 60% B; 52–57 min, 60% B; 58–65 min, 100% B. Fluorescence detection was carried out with excitation and emission wavelengths set at 320 nm and 420 nm, respectively. Peaks were identified using the standard panel and polysaccharide digest control as retention time standards and the abundances were quantified manually by peak area.

Patch clamp electrophysiology. *Npy*-GFP male mice were placed on a HFHS diet for 12 weeks before being stereotaxically injected with either vehicle or chABC in the ARC 3 days before electrophysiological characterization. Mice were anaesthetized with isoflurane prior to brain extraction, and brains were incubated in ice-cold artificial cerebrospinal fluid (aCSF) of the following composition: 127 mM NaCl, 1.2 mM KH₂PO₄, 1.9 mM KCl, 26 mM NaHCO₃, 3 mM D-glucose, 7 mM mannitol, 2.4 mM CaCl₂, 1.3 mM MgCl₂ (saturated with 95% O₂ and 5% CO₂, pH 7.4). Coronal sections (250 µm) of the ARC were cut using a vibratome (Leica VTS1000S). Slices were heated for 30 min at 34 °C and then allowed to cool to room temperature prior to recording. Slices were placed in a recording chamber and continuously perfused with room temperature aCSF.

Npy-GFP neurons in the ARC were visualized using fluorescence and differential interference contrast optics with infrared video microscopy (AxioCam MRM, Zeiss) and an upright microscope (BX51WI, Olympus). For current clamp recordings, patch pipettes (8–11 MΩ) were pulled from thin-walled borosilicate glass (Sutter Instruments, BF150-86-10) using a horizontal puller (Sutter Instruments) and filled with intracellular solution containing 140 mM potassium gluconate, 10 mM HEPES, 10 mM KCl, 1 mM EGTA, 4 mM Na-ATP, 0.3 mM Na-GTP and 10 mM Biocytin (300 mOsm and pH 7.3, with osmolality and pH adjusted with sucrose and KOH accordingly). In voltage-clamp recordings to examine K⁺ currents, patch pipettes (3–6 MΩ) were filled with intracellular solution containing 130 mM potassium gluconate, 6 mM NaCl, 4 mM NaOH, 11 mM EGTA, 1 mM CaCl₂, 10 mM HEPES, 1 mM MgCl₂, 2 mM Na-ATP, 0.2 mM Na-GTP, 0.1% biocytin (295 mOsm and pH 7.3, with osmolality and pH adjusted with sucrose and KOH accordingly). Cells with a series resistance of >20 MΩ were not included in the analysis. Recordings were made in the presence of tetrodotoxin, where 11 depolarizing pulses applied from –40 to +60 mV for 500 ms in 10 mV increments from a holding potential of –80 mV. A 50 ms prepulse to 0 mV was used to inactivate any residual voltage-dependent Na⁺ current. Whole-cell recordings were made using a Double IPA Integrated Patch amplifier controlled with SutterPatch software (Sutter Instruments) with all current clamp data filtered at 5 kHz. Data were analysed using Sutterpatch (Sutter Instruments) and Clampfit 10.7 (Axon Instruments).

Immunoblotting

The mediobasal hypothalamus was microdissected and snap frozen in liquid nitrogen. Tissues were mechanically homogenized in 100 µl ice-cold RIPA lysis buffer (ab156034, Abcam, UK, containing PhosStop Phosphatase Inhibitor, 1 tablet per 10 ml; Roche PHOSS-RO) and clarified by centrifugation (13,000 rpm for 20 min at 4 °C). Tissue

lysates were resolved by SDS-PAGE and immunoblotted as described previously (PMID: 31509751). Antibodies used are rabbit phospho-IR (Tyr1162, Tyr1163) polyclonal antibody (1:1,000, 44–804 G, Invitrogen, MA), rabbit monoclonal anti-IR (1:1,000, 3025x, Cell Signaling), rabbit-β-actin polyclonal antibody (1:2,000, 4967, Cell Signaling Technology), mouse GAPDH monoclonal antibody (1:5,000, 60004-1-Ig, Proteintech), mouse monoclonal anti-tubulin (1:2,000, T5168, Sigma).

Real-time PCR

RNA was extracted using TRIzol reagent (Invitrogen) and total RNA quality and quantity determined using a NanoDrop 3300 v2.8.1 (Thermo Scientific). mRNA was reverse-transcribed using a High-Capacity cDNA Reverse Transcription Kit (Applied Biosystems) and processed for quantitative real-time PCR using SYBR Green PCR Master Mix (4309155, Applied Biosystems). The following primers were used for SYBR green expression assays: *Adamst4* (forward-GAACGGTGGCAAGTATTGTGAGG, reverse-TTCGGTGGTTGTAGGCAGCACA), *Adamst5* (forward-CTGCCTTCAAGGCAATGTGTGG, reverse-CAATGGCGGTAGGCAAACCTGCA), *Ikkb* (forward-GCAGACTGACATTGTGGACCTG, reverse-ATCTCC TGGCTGTACCTTCTG), *Il6* (forward-GGTGCCCTGCCAGTATTCTC, reverse-GGCTCCCAACACAGGATGA), *Kcna4* (forward-GCAGAT TGCTGAATGACACCTCG, reverse-GGACAAGCAAAGCATCGAACCCAC), *Kcnb1* (forward-GAGGAGTTCGACAACACGTGCT, reverse-TGAGTG ACAGGGCAATGGTGGA), *Kcnb2* (forward-GCTGGAGAAACCTAA CTCGTCC, reverse-CTCGTCGTTTTCTTCGAGCTCTG), *Kcnc3* (forward-GAAGAGGTGATTGAAACCAACAGG, reverse-TGGGCTCTTGTCTTCT GGAGAC), *Kcnc4* (forward-CCAGCTCGAATCGCCCATTTAC, reverse-AGCACCATTAGCATCGCCAT), *Kcnd2* (forward-CCTACATGCAGAG CAAGCGGAA, reverse-GTGGTTTTCTCCAGGCAGTGAAG), *Kcnd3* (forward-AGAAGAGGAGCAGATGGGCAAG, reverse-CTTGATGGTGGAGG TTCGTACAG), *Kcnj11* (forward-TGCGTCAAGCATCCACTCTCT, reverse-GGACATTCCTGTCCACCATGC), *Kcnj3* (forward-CAGTTCGAGGT TGTCGTATCC, reverse-CCCAAAGCACTTCGTCCTCTGT), *Kcnj6* (forward-GGAACTGGAGATTGTGGTATCC, reverse-TCTTCCAGCG TTAGGACAGGTG), *Kcnj9* (forward-TCTCACCTCTCGTCATCAGCCA, reverse-GCTTCGAGCTTGGCACGTCATT), *Kcnma1* (forward-CCTGAAGGACTTTCTGCACAAGG, reverse-ACTCCACCTGAGTGAA ATGCCG), *Kcnn3* (forward-TCCACCCTCATCCTGCTTGGTT, reverse-CAGGCTGATGATAGGATACGC), *Kcnq3* (forward-AAGCCTACGCTTTC TGGCAGAG, reverse-ACAGCTCGGATGGCAGCCTTTA), *Mmp13* (forward-AGCAGTTCAAAGGCTACAACCT, reverse-GGATGCTTAGGGTTGGGGTC), *Mmp14* (forward-AGCACTGGGTGTTGACGAA, reverse-CCGGTAGT ACTTATTGCCCCCG), *Mmp2* (forward-GTCGCCCTAAAACAGACAA, reverse-GGTCTCGATGGTGTCTGGT), *Mmp9* (forward-GCTGACTAC GATAAGGACGGCA, reverse-TAGTGGTGCAGGCAGAGTAGGA), *Nfkb1* (forward-GCTGCCAAAAGAAGGACACGACA, reverse-GGCAGGCTAT TGCTCATCACAG), *Rn18s* (forward-CAGCTCCAAGCGTTCCTGG, reverse-GGCCTTCAATTACAGTCGTCTTC), *sTgfr2* (forward-AAGGTTTCAGCT ACACCTT, reverse-GTCGGGACTGCTGGTGGTGT), *sTnfr1α* (forward-GG TTATCTTGCTAGGTCTTTG, reverse-GATCCCTACAAATGATGGAG), *Tgfb1* (forward-GGATACCAACTATTGCTTCAG, reverse-TGTCCAGGCTCC AAATATAG), *Tgfb2* (forward-CTAATGTTGTGTGCCCTCTACAG, reverse-GCACAGAAGTTAGCATTGTATCCC), *Tgfb1* (forward-GGACC ATTGTGTTACAAGAAAGC, reverse-CATGGCGTAACATTACAGTCTGA), *Tgfb2* (forward-TCCTAGTGAAGAAGCACTTGACC, reverse-TACCAGA GCCATGGAGTAGACAT), *Timp1* (forward-TCTTGGTTCCCTGGCGTA CTCT, reverse-GTGAGTGTCACTCTCCAGTTTGC), *Timp3* (forward-GCT AGAAGTCAACAAATACCAG, reverse-TAGTAGCAGGACTTGATCTTG) and *Tnf* (forward-CTGTGAAGGGAATGGGTGTT, reverse-GGTCACTGTCCC AGCATCTT).

Gene expression was normalized to *Rn18s* and relative quantification was achieved using the $\Delta\Delta C_T$ method. Reactions were performed using a Bio-Rad CFX 384 touch (Bio-Rad).

PNN binding assay

To determine the interaction of insulin with PNN components *in vitro*, flat-bottom 96-well plates were first coated with 10 $\mu\text{g ml}^{-1}$ poly-L-lysine overnight, followed by a rinsing with water. A purified CSPGs mix containing neurocan, phosphacan, versican and aggrecan (CC117, Merk Millipore), purified aggrecan (A1960, Merk Millipore) or purified C4S (S9004, Selleck Chemicals), were coated onto the 96-well plates at a concentration of 10 $\mu\text{g ml}^{-1}$ for 4 h at room temperature, followed by a rinse with water. Insulin-FITC was incubated on plates containing ECM at concentration ranging from 5–1 mg ml^{-1} for 2 h at room temperature and protected from light. Control wells contained either no ECM, bovine serum albumin (10 $\mu\text{g ml}^{-1}$) or poly-L-lysine alone. Wells were washed 3 times with water and imaged using a SPECTROstar Nano Microplate Reader (BMG Labtech, Germany). To digest PNN or to negate PNN negative charge, wells were incubated with either chABC (0.5 U ml^{-1}) or poly-L-arginine (10 $\mu\text{g ml}^{-1}$, P7762, Merk Millipore) for 1 h at 37° C after the ECM coating, washed 3 times with water and then incubated with insulin-FITC.

Statistics and Reproducibility

Statistical analyses were performed using GraphPad Prism version 10 (GraphPad Software). Statistical significance was determined by a one-way or two-way ANOVA with multiple comparisons or repeated-measures, one or two-tailed paired or unpaired Student's *t*-tests, ANCOVA, or simple linear regression as appropriate. $P < 0.05$ was considered significant: * $P < 0.05$, ** $P < 0.01$ and *** $P < 0.001$. Statistical details of individual experiments such as exact values of *n* and exact statistical tests can be found in figures and legends.

Reporting summary

Further information on research design is available in the Nature Portfolio Reporting Summary linked to this article.

Data availability

Source data are provided with this paper.

47. Arnst, N. et al. Spatial patterns and cell surface clusters in perineuronal nets. *Brain Res.* **1648**, 214–223 (2016).

48. Lee, H., McKeon, R. J. & Bellamkonda, R. V. Sustained delivery of thermostabilized chABC enhances axonal sprouting and functional recovery after spinal cord injury. *Proc. Natl Acad. Sci. USA* **107**, 3340–3345 (2010).
49. Alonge, K. M. et al. Hypothalamic perineuronal net assembly is required for sustained diabetes remission induced by fibroblast growth factor 1 in rats. *Nat. Metab.* **2**, 1025–1033 (2020).
50. Dodd, G. T. et al. Intranasal targeting of hypothalamic PTP1B and TCPTP reinstates leptin and insulin sensitivity and promotes weight loss in obesity. *Cell Rep.* **28**, 2905–2922. e2905 (2019).
51. Sartori, R. et al. Perturbed BMP signaling and denervation promote muscle wasting in cancer cachexia. *Sci. Transl. Med.* **13**, eaay9592 (2021).
52. Blankinship, M. J. et al. Efficient transduction of skeletal muscle using vectors based on adeno-associated virus serotype 6. *Mol. Ther.* **10**, 671–678 (2004).
53. Moh, E. S. X. et al. Long-term intrathecal administration of morphine vs. baclofen: differences in CSF glycoconjugate profiles using multiglycomics. *Glycobiology* **32**, 50–59 (2022).

Acknowledgements The authors thank B. Boztepe, A. Jobling, J. Ivanusic, S. Dodd, G. Dodd and L. Bowers for feedback on this work and reagents alongside members of the Dodd, Watt and Parker laboratories for discussions. We also thank L. Bowers for help with generating Image J macros; R. Lee-Young for help with the hyperinsulinaemic–euglycaemic clamp technique; S. McDougall for electrophysiological support; C. Goodman and H. Qian for assistance with AAV vectors generation; and J. Bhandari for genotyping. This project relied on the Melbourne Mouse Metabolic Phenotyping Platform for experiments in metabolic cages, the Biological Optical Microscopy Platform and the Melbourne Histology Platform at The University of Melbourne for microscopy and histology. This work was funded by NHMRC Grants 2022/GNT2021126, 2020/GNT2002427 and 2018/GNT1160043; Australian Research Council Grants DP220102910 and CE200100029; Diabetes Australia Grants Y23G-DodG and Y20G-DodG; The University of Melbourne Deans Innovation Award; a Baillieu Research Scholarship; a Graduate Women Victoria Scholarship; and an NHMRC Investigator Grant (APP2017070 and APP2009642).

Author contributions G.T.D. conceived the study, and designed, performed and analysed experiments. C.A.B. designed, performed and analysed experiments and wrote the code to analyse images of brain sections. F.S., A.L.H., S.D. and E.S.X.M. performed and analysed experiments. V.W.Y. and C.-C.L. advised on the study, and alongside P.Z., synthesized fluorosamine. E.C., K.L., A.J.R., M.K.M., N.H.P., M.W., B.L.P., R.M.B., P.G. and C.K. advised on the study and provided samples for analyses and/or reagents. G.T.D. obtained funding for the research. G.T.D. and C.A.B. wrote the manuscript.

Competing interests G.T.D., C.A.B. and F.S. hold method-of-use patents for treating insulin resistance and associated disorders (patent numbers WO2024086895 and WO2024113004).

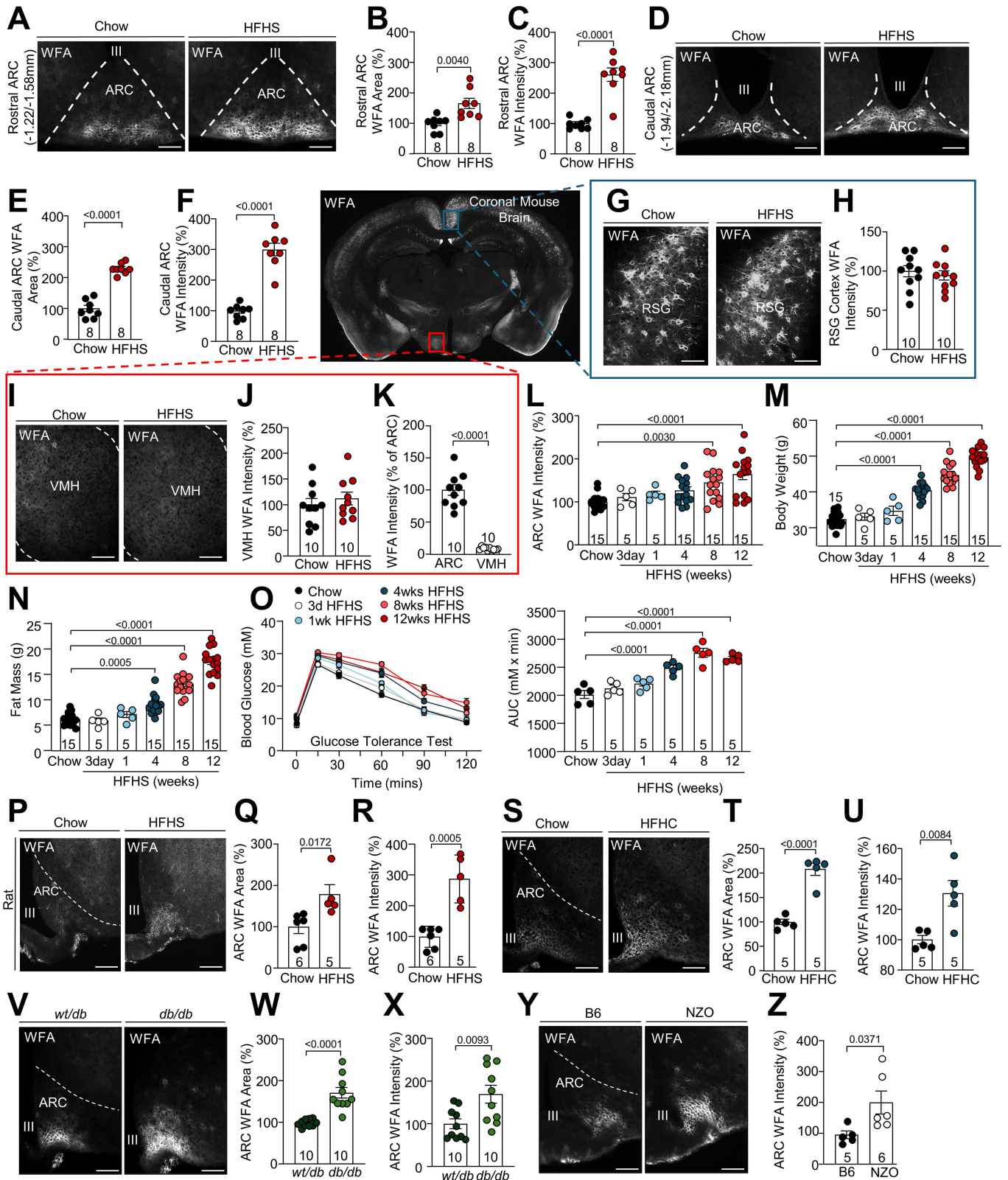
Additional information

Supplementary information The online version contains supplementary material available at <https://doi.org/10.1038/s41586-024-07922-y>.

Correspondence and requests for materials should be addressed to Garron T. Dodd.

Peer review information Nature thanks Alexander Dityatev and the other, anonymous, reviewer(s) for their contribution to the peer review of this work.

Reprints and permissions information is available at <http://www.nature.com/reprints>.

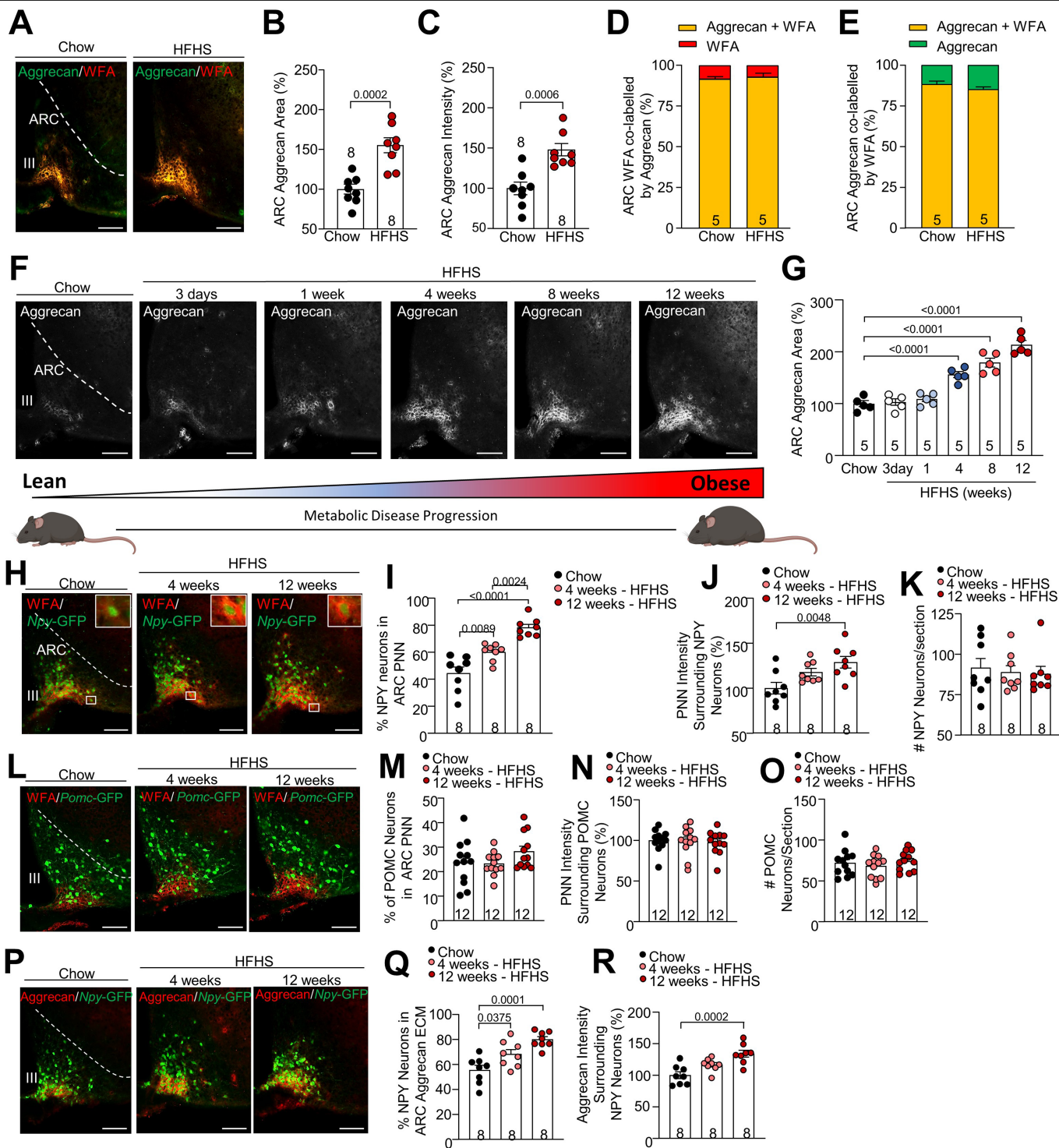


Extended Data Fig. 1 | See next page for caption.

Article

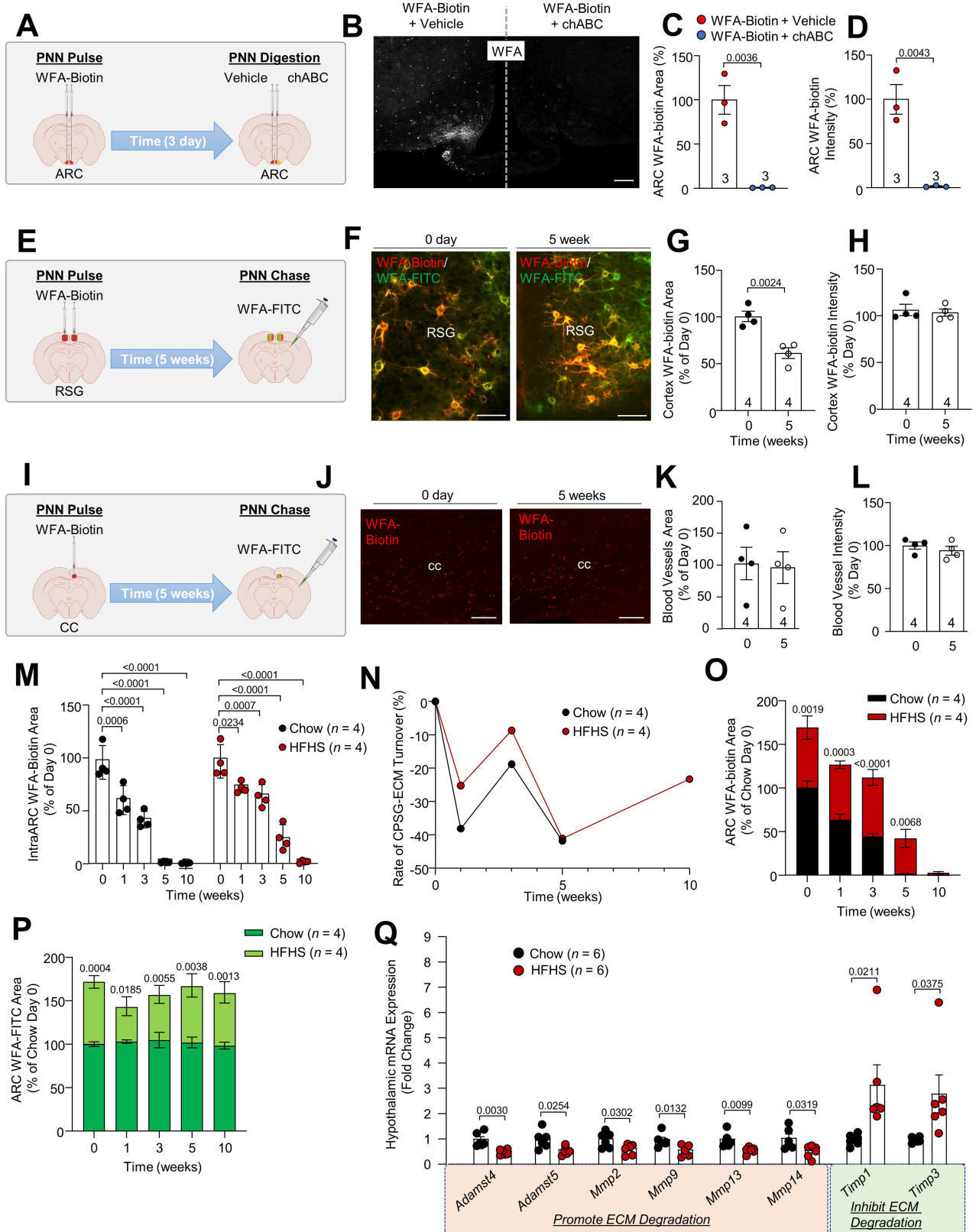
Extended Data Fig. 1 | The development of neurofibrosis within the ARC across dietary and genetic models of obesity. Aged-matched C57BL/6 J mice were fed a chow or HFHS diet for 12 weeks and brains were processed for immunohistochemistry monitoring for WFA. Staining area and intensity was quantified in the **a-c)** rostral ARC, **d-f)** caudal ARC, **g,h)** RSG and **i-k)** VMH. C57BL/6 J mice were fed HFHS diet for 0, 3 days, 1, 4, 8 or 12 weeks and **l)** the PNN intensity in the ARC, **m)** body weight, **n)** fat mass and **o)** glucose tolerance were assessed. **p-r)** Sprague Dawley rats were fed a chow or HFHS or **s-u)** C57BL6/J mice fed a chow or HFHC diet for 12 weeks or 30 weeks, respectively, and brains were processed for WFA immunostaining and **q,t)** area and **r,u)** intensity within

the ARC quantified. Brains from chow fed **v-x)** obese *db/db* or non-obese *wt/db* controls and **y,z)** obese NZO or non-obese B6 controls were processed for WFA immunostaining. Results are mean \pm SEM; significance was determined using **b, c, e, f, k, q, r, t, u, w, x, z)** two-tailed t-test, or **l-o)** one way ANOVA with multiple comparisons. **n** = biologically independent samples and significance is representative of at least three independent experiments. Scale bar, 100 μ m. **Abbreviations:** III, 3rd ventricle; ARC, arcuate nucleus of the hypothalamus; HFHC, high-fat high-cholesterol; HFHS, high-fat high-sugar diet; NZO, New Zealand Obese mouse; RSG, Retrosplenial cortex; VMH, ventromedial hypothalamus; WFA, *Wisteria Floribunda* Lectin; AUC, area under the curve.



Extended Data Fig. 2 | Obesity driven ARC neurofibrosis is underscored by compositional changes in the PNN. **a**) Aged-matched C57BL/6J mice were fed a chow or HFHS diet for 12 weeks and brains were processed for aggrecan immunostaining; **b**) area, **c**) intensity and **d**), **e**) co-expression within the ARC was quantified. **f**) C57BL/6J mice were fed HFHS diet for 0, 3 days, 1, 4, 8 or 12 weeks and brains were processed for aggrecan immunohistochemistry and **g**) staining area was quantified. **h-k**), **p-r**) *Npy*-GFP and **l-o**) *Pomc*-EGFP mice were HFHS fed for 0, 4 and 12 weeks and brains processed for **h-o**) WFA or **p-r**) aggrecan immunostaining. **k**), **o**) Cell number, **i**), **m**), **q**) staining encased cell

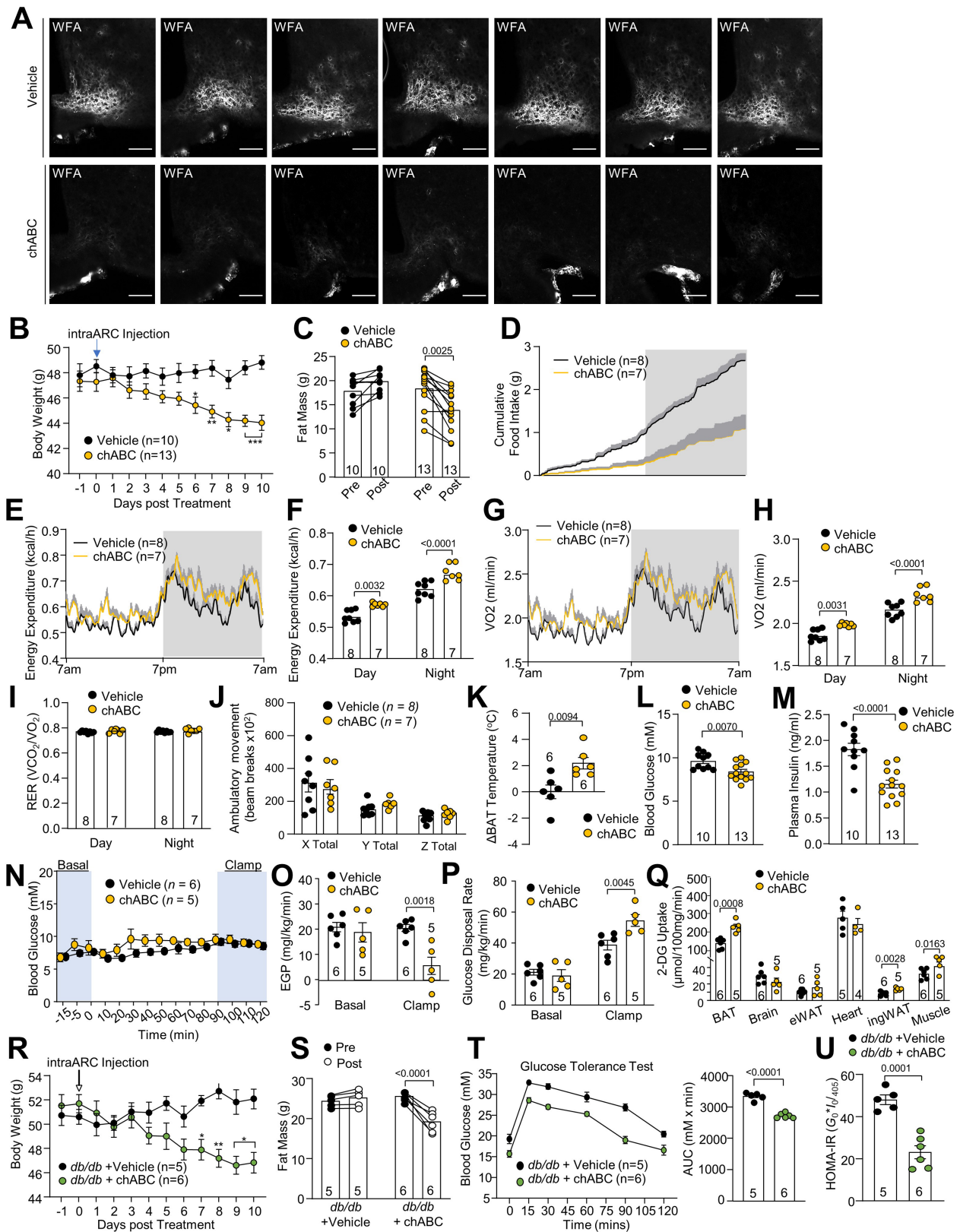
number, and **j**), **n**), **r**) surrounding staining intensity was quantified. Results are mean \pm SEM; significance determined using **b**), **c**) two-tailed t-test, and **g**), **i-r**) one-way ANOVA with Tukey's multiple comparisons. n = biologically independent samples and significance represents at least two independent experiments. Scale bar, 100 μ m. **Abbreviations:** III, 3rd ventricle; ARC, arcuate nucleus of the hypothalamus; GFP, green fluorescent protein; HFHS, high-fat high-sugar diet; NPY, neuropeptide-Y; PNN, perineuronal net; POMC, pro-opiomelanocortin; WFA, *Wisteria Floribunda* Lectin.



Extended Data Fig. 3 | See next page for caption.

Extended Data Fig. 3 | Validation of PNN Tracker. a-b) 8-week-old C57BL/6 J mice received bilateral administration of WFA-biotin into the ARC. 3-days post injection mice received further unilateral administration of vehicle or chABC into the ARC. 1- day later brains were extracted and processed for WFA immunohistochemistry and staining **c)** area and **d)** intensity was quantified. 8-week old C57BL/6 J mice received **e-h)** bilateral administration of WFA-biotin into the RSG or **i-l)** unilateral administration of WFA-biotin into the cc. 0- and 5-weeks post injection brains were extracted and subjected to WFA immunohistochemistry and staining **g,k)** area and **h, l)** intensity was quantified. 12-week HFHS-fed or aged-matched chow C57BL/6 J male mice received bilateral administration of WFA-biotin into the ARC. Brains were extracted 0 days, 1-, 3-, 5- or 10-weeks post-injection, processed for WFA

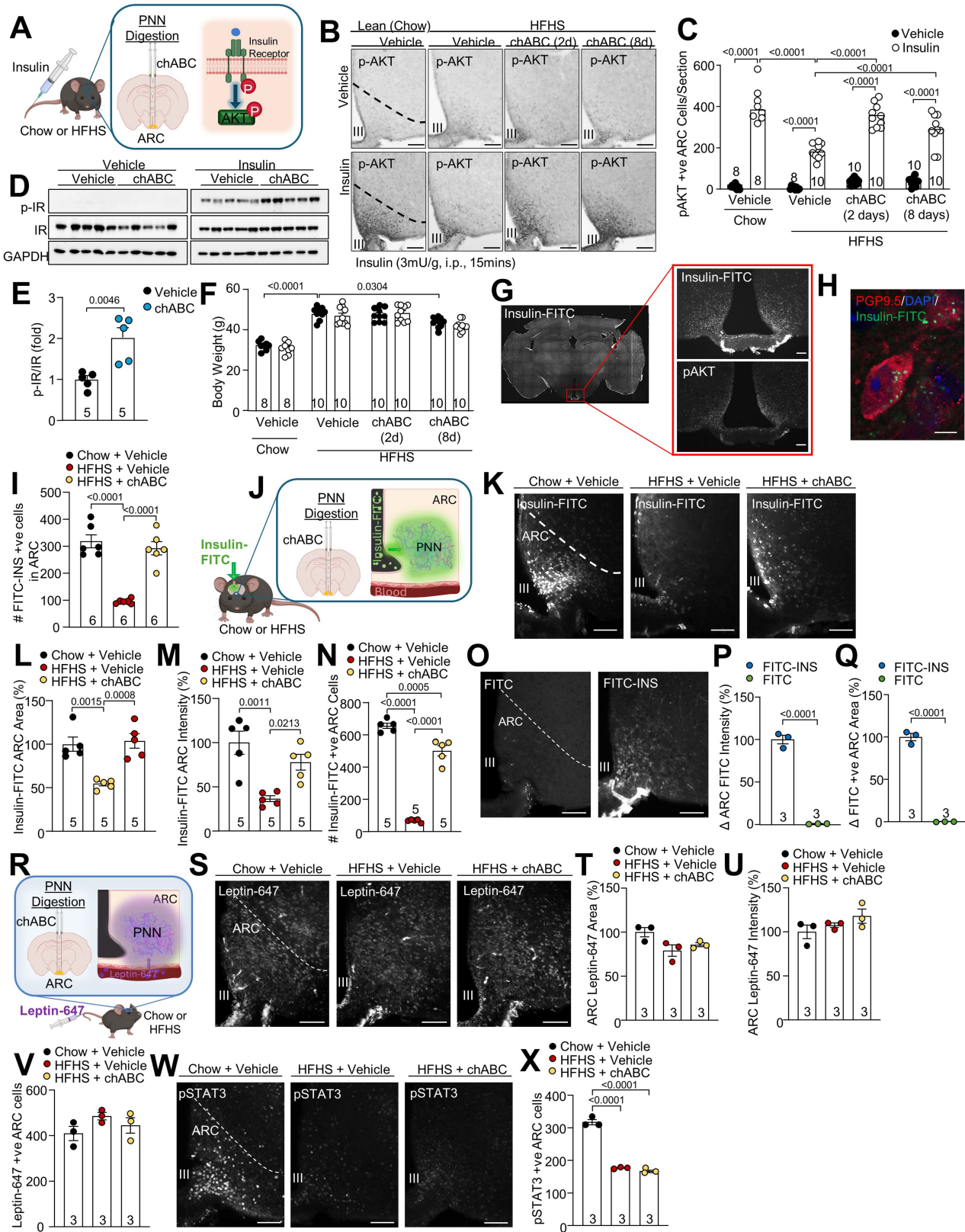
immunohistochemistry and **m, n)** PNN turnover, **o)** WFA-biotin area, **p)** WFA-FITC was quantified within the ARC. **q)** Extracellular matrix regulation enzymes gene expression was determined in the mediobasal hypothalamus from 12-week diet-induced obese or aged-matched chow C57BL/6 J male mice. Results are mean \pm SEM; significance determined using **c, d, g, o, p, q)** two-tailed t-test, **m)** one-way ANOVA with Dunnett's multiple comparisons. *n* = biologically independent samples and significance is representative of at least two independent experiments. Scale bar, 100 μ m. *Abbreviations:* ARC, arcuate nucleus of the hypothalamus; cc, corpus collosum; PNN, perineuronal net; FITC, Fluorescein isothiocyanate; HFHS, high-fat high-sugar diet; RSG, Retrosplenial cortex; WFA, *Wisteria Floribunda* Lectin.



Extended Data Fig. 4 | See next page for caption.

Extended Data Fig. 4 | Effects of enzymatic attenuation of neurofibrosis on metabolism and glucose homeostasis. C57BL/6 J mice were fed a HFHS diet for 12 weeks and bilaterally injected with vehicle or chABC into the ARC. **a)** Representative images of PNN expression from individual mice 10 days post intraARC injection of vehicle or chABC. **b)** Body weight, **c)** adiposity, **d)** cumulative food intake, **e, f)** energy expenditure, **g, h)** oxygen consumption, **i)** RER, **j)** ambulatory activity, **k)** BAT dermal thermography, **l)** fasted blood glucose and **m)** fasted plasma insulin was measured. Hyperinsulinemic-euglycemic clamps were performed in HFHS fed mice bilaterally intraARC injected with vehicle or chABC. Results are shown for **n)** blood glucose, **o)** EGP, **p)** glucose disposal rate and **q)** tissue specific insulin-stimulated

uptake. 15-week-old *db/db* mice were bilaterally injected with vehicle or chABC into the ARC. **r)** Body weights, **s)** adiposity, **t)** glucose tolerance and **u)** HOMA-IR was assessed. Results are mean \pm SEM; significance determined using **b, c, f, h, o, r, s,)** two-way ANOVA with multiple comparisons test and **k, l, m, p, t, u)** two-tailed t-test. *n* = biologically independent samples and significance is representative of at least two independent experiments. Scale bar, 100 μ m. **Abbreviations:** 2-DG, [14 C] 2-deoxyglucose; BAT, Brown adipose tissue; chABC, chondroitinase ABC; EGP, endogenous glucose production; HFHS, high-fat high-sugar diet; PNN, perineuronal net; RER, Respiratory exchange ratio; WFA, *Wisteria Floribunda* Lectin.

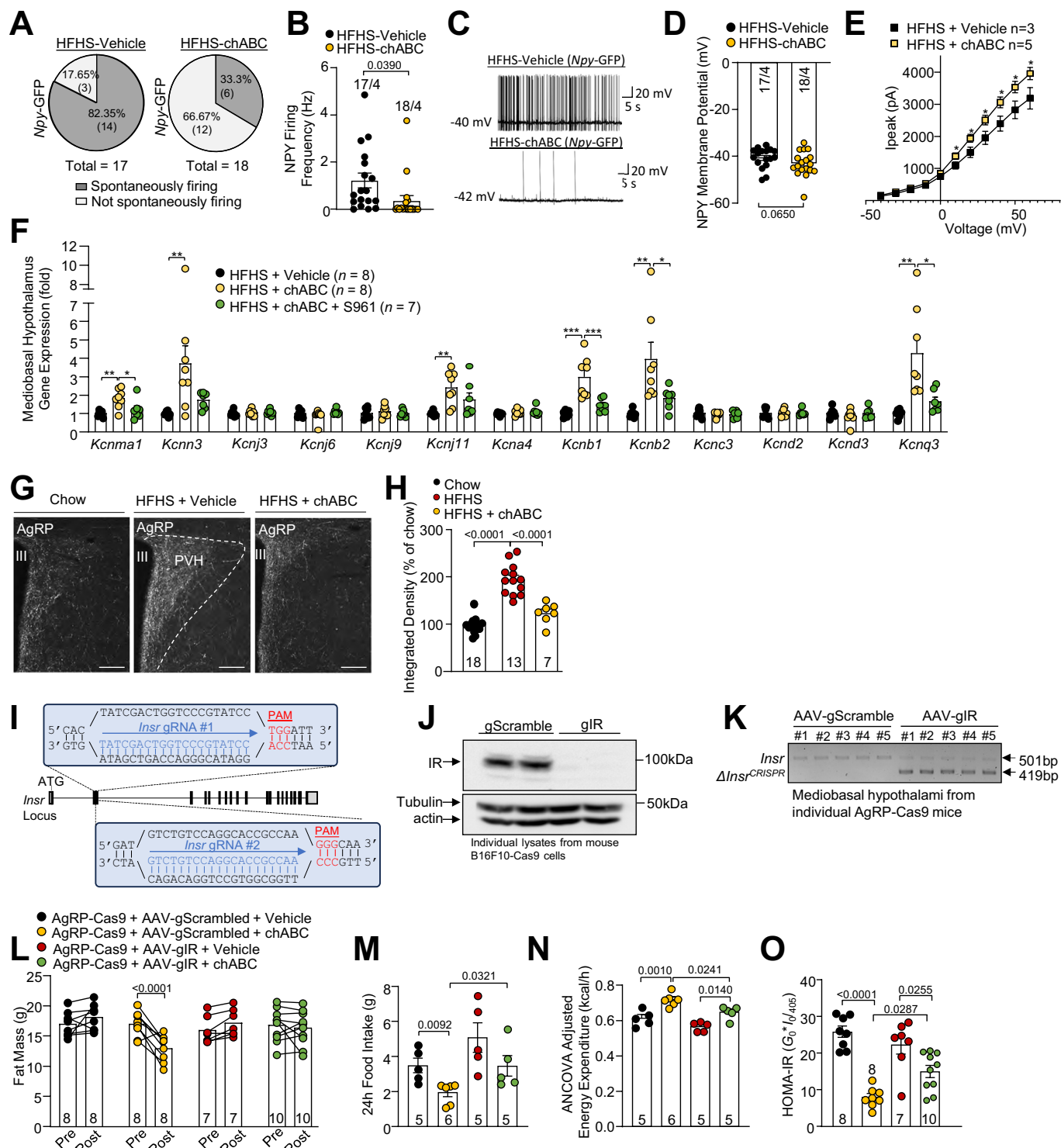


Extended Data Fig. 5 | See next page for caption.

Extended Data Fig. 5 | Neurofibrosis interacts with insulin in the ARC.

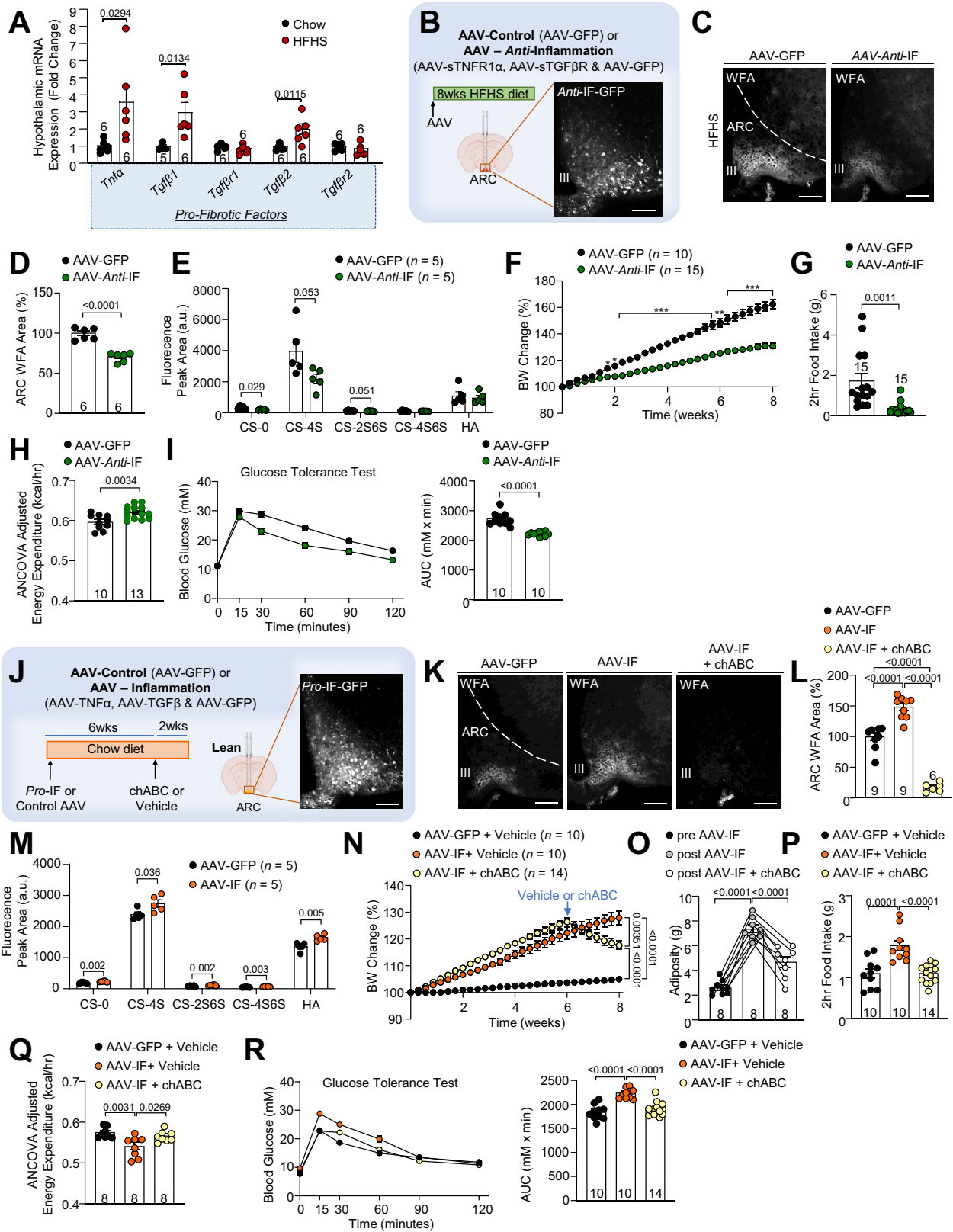
a) C57BL/6 J mice were fed a chow or HFHS diet for 12 weeks and bilaterally injected with vehicle or chABC into the ARC and hypothalami were processed for **b-e)** insulin-induced p-AKT expression and **f)** body weights. **g)** Image demonstrating insulin-FITC and signaling within the ARC. Chow or HFHS C57BL/6 J mice were bilaterally intraARC injected with vehicle or chABC. 4-days post-ARC injection, mice administered with **h,i)** insulin-FITC or **r)** leptin-647. **h)** Representative image and **i)** quantification of insulin-FITC internalization into ARC neurons. **s)** ARC leptin-647 expression was quantified by **t)** area, **u)** intensity **v)** number of leptin-647 positive ARC cells and **w,x)** pSTAT3 cells. **j)** Lateral ventricle administered insulin-FITC, **k)** expression, **l)** area, **m)** intensity and **n)** number of insulin-FITC positive cells was quantified. **o-q)** Mice were

administered FITC or insulin-FITC and fluorescent **p)** area and **q)** intensity was quantified. Results are mean \pm SEM; significance determined using **e, p, q)** two-tailed t-test and **c, f, i, l, m, n, x)** one-way ANOVA with Tukey's multiple comparisons. Scale bar, 100 μ m. **n** = biologically independent samples. **h)** Scale bar, 5 μ m. *Abbreviations:* III, 3rd ventricle; ARC, arcuate nucleus of the hypothalamus; chABC, chondroitinase ABC; PNN, perineuronal net; DAPI, 4',6'-diamidino-2-phenylindole; FITC, Fluorescein isothiocyanate; GAPDH, Glyceraldehyde 3-phosphate dehydrogenase; HFHS, high-fat high-sugar diet; IR, Insulin Receptor; p-AKT, AKT Ser-473 phosphorylation; p-STAT3, phosphorylated signal transducer and activator of transcription 3; PGP9.5, Protein gene product 9.5; p-IR, phosphorylated IR.



Extended Data Fig. 6 | Neurofibrosis regulates AgRP neuronal activity in obesity via insulin signaling deficits. Whole-cell patch clamp electrophysiology in NPY neurons of HFHS *Npy*-GFP mice following intraARC vehicle or chABC. **a)** Proportion of spontaneously firing neurons, **b,c)** firing frequency **d)** resting membrane potential and **e)** IV curve showing K⁺ currents. C57BL/6J mice were fed a chow or HFHS diet and bilaterally intraARC injected with vehicle or chABC. **f)** 3 days later mice were administered vehicle or IR antagonist (S961) and mediobasal hypothalamic gene expression quantified. **g,h)** PVH AgRP immunoreactivity was quantified **i)** CRISPR guide RNA strategy targeting the mouse IR gene. **j)** IR knockout was determined using western blotting and **k)** PCR detecting the presence of CRISPR-mediated excision ($\Delta Insr^{CRISPR}$). 12-week HFHS fed AgRP-Cas9 mice received bilateral intraARC injections of AAV-gScrambled or AAV-gIR, and 1-week later mice

received bilateral injections of vehicle or chABC to disassemble neurofibrosis in the ARC. **l)** Adiposity, **m)** food intake, **n)** energy expenditure and **o)** HOMA-IR was assessed. Results are mean \pm SEM; significance determined using b, m) unpaired t-tests (two-tailed), d) unpaired t-tests (one-tailed), f, h, n, o) one-way ANOVA with Tukey's multiple comparisons, e) two-way ANOVA with Holm-Šidák's multiple comparisons and l) two-way ANOVA with Tukey's multiple comparisons test. n = biologically independent samples and significance represents at least two independent experiments. Scale bar, 100 μ m. **Abbreviations:** III, 3rd ventricle; AgRP, agouti-related peptide; ARC, arcuate nucleus of the hypothalamus; chABC, chondroitinase ABC; GFP, green fluorescent protein; HFHS, high-fat high-sugar diet; HOMA-IR, Homeostatic Model Assessment for Insulin Resistance; IR, Insulin Receptor; NPY, neuropeptide-Y; PNN, perineuronal net; PVH, paraventricular hypothalamus; WFA, *Wisteria Floribunda* Lectin.

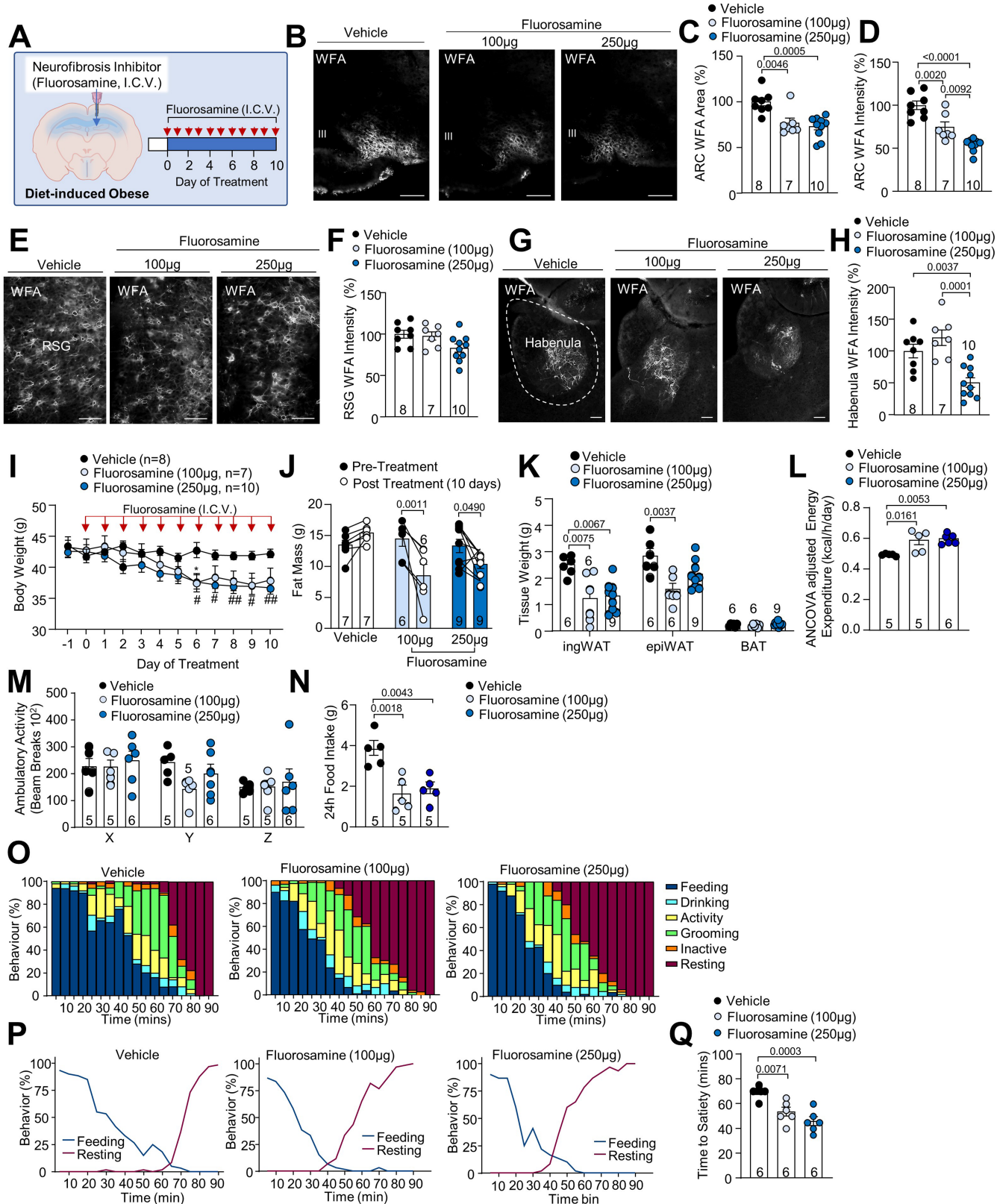


Extended Data Fig. 7 | See next page for caption.

Article

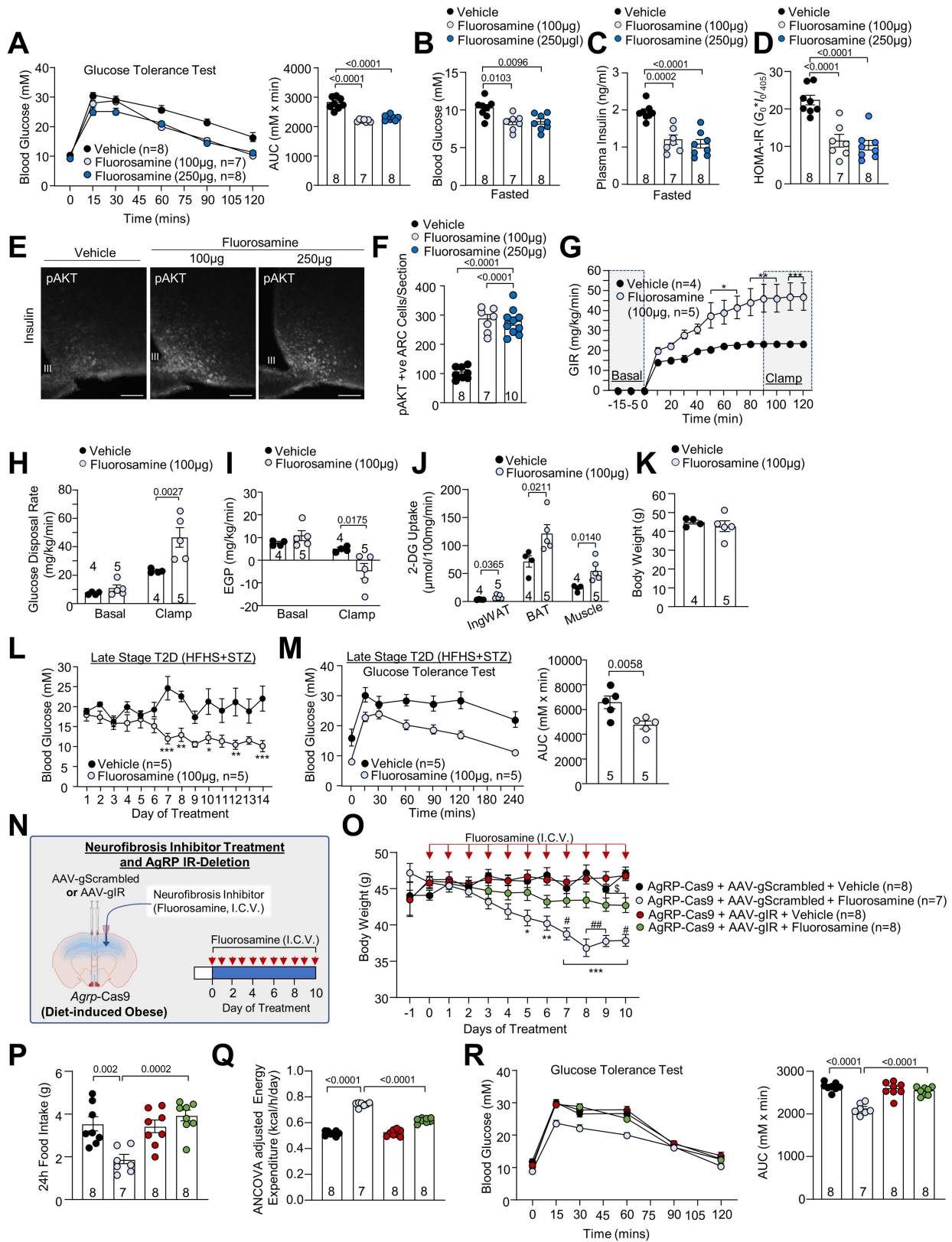
Extended Data Fig. 7 | Inflammation drives ECM remodeling within the ARC to promote metabolic dysfunction. **a)** C57BL/6 J mice were fed a HFHS diet for 12 weeks and brains were extracted for assessment of pro-fibrotic gene expression. **b)** 10-week-old C57BL/6 J mice received bilateral intraARC injections of *anti*-inflammatory AAV vectors expressing soluble receptors for TNFR1 α and TGF β R or control, before being placed on a HFHS for 8-weeks. Brains were extracted and processed for **c,d)** ARC WFA immunofluorescence and **e)** CS-GAG abundance. **f)** Body weight, **g)** fasting induced 2-hour food intake, **h)** energy expenditure and **i)** glycemic control were assessed. **j)** 10-week-old C57BL/6 J mice received bilateral injections into the ARC to administer inflammatory AAV vectors expressing TNF α and TGF β ligands, or control. 6-weeks later mice received bilateral intraARC injections of vehicle or chABC to enzymatically

digest the ARC PNN and **k,l)** brains were processed for WFA immunostaining or **m)** quantitative analysis of CS-GAG abundance. **n)** Body weight, **o)** adiposity, **p)** fasting induced 2-hour food intake, **q)** energy expenditure and **r)** glycemic control was assessed. Results are mean \pm SEM; significance determined using **o, p, q, r)** one-way ANOVA with Tukey's multiple comparisons, **f, n)** two-way ANOVA with multiple comparisons, **a, d, e, g, h, i, m)** two-tailed t-tests. **n** = biologically independent samples and significance is representative of two independent experiments. Scale bar, 100 μ m. *Abbreviations:* III, 3rd ventricle; ARC, arcuate nucleus of the hypothalamus; AUC, area under the curve; BW, body weight; chABC, chondroitinase ABC; CS-GAG, chondroitin sulfate glycosaminoglycans; GFP, green fluorescent protein; HA, hyaluronan acid; HFHS, high-fat high-sugar diet; IF, inflammatory; WFA, *Wisteria Floribunda* Lectin.



Extended Data Fig. 8 | Pharmacologically targeting neurofibrosis promotes weight loss in obesity. a) 12-week HFHS fed male C57BL/6J mice received daily I.C.V. administration of vehicle or fluorosamine for 10 days. PNN expression in the b-d) ARC, e,f) RSG and g,h) habenula was assessed. Effects on i) body weight, j,k) adiposity, l) energy expenditure, m) ambulatory activity, and n) food intake was assessed. HFHS fed mice received I.C.V. administration of vehicle or fluorosamine (100 or 250 µg/animal) for 10 consecutive days, fasted overnight then given access to food *ad libitum* and o) behaviour, p)

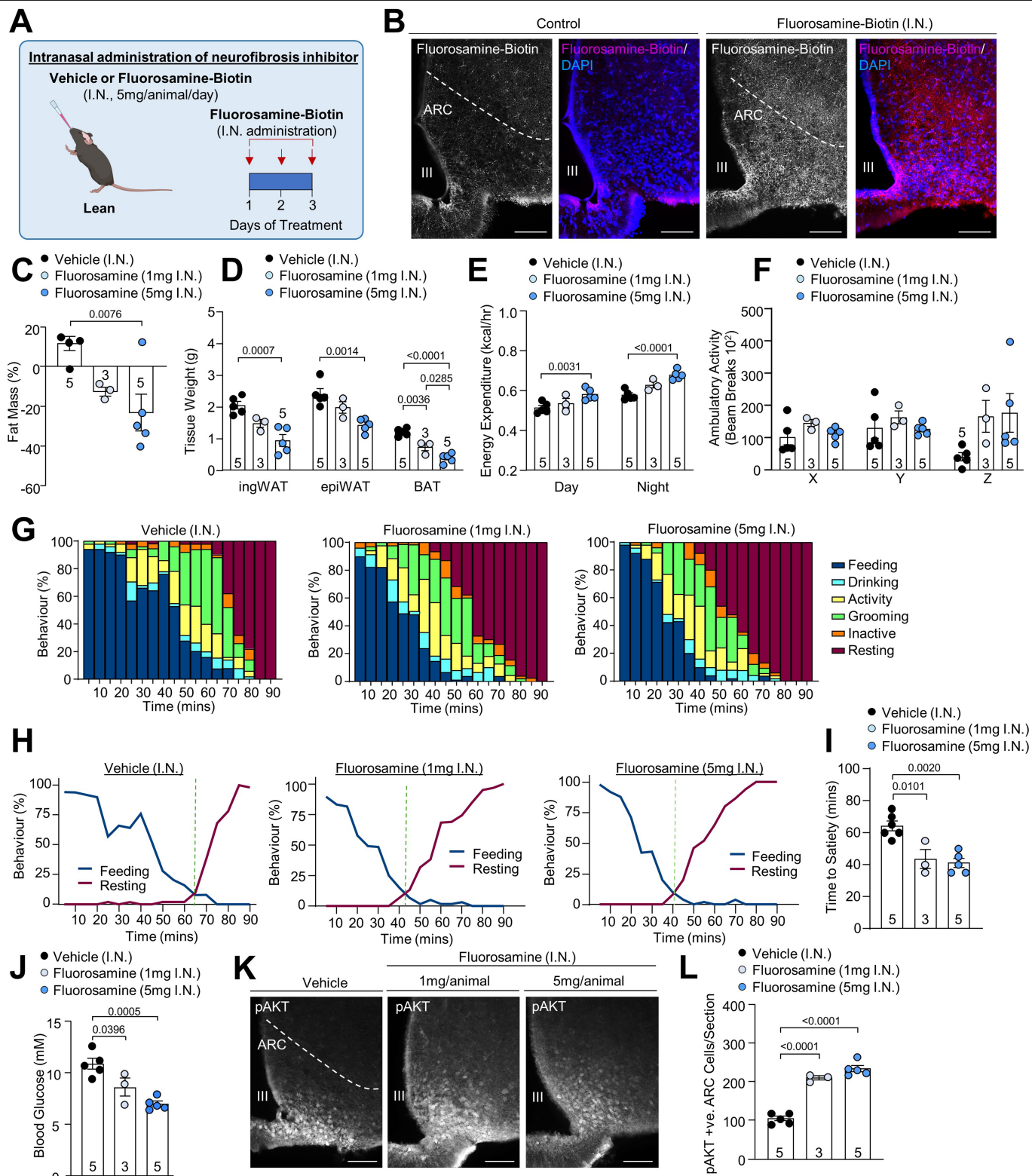
transition point from feeding to resting/satiety and q) the time to satiety was determined. Results are mean \pm SEM. Significance determined c, d, h, k, l, n, q) one-way ANOVA with Tukey's multiple comparisons, i) two-way ANOVA with multiple comparisons. n = biologically independent samples and significance is representative of at least two independent experiments. Scale bar, 100 µm. **Abbreviations:** III, 3rd ventricle; HFHS, high-fat high-sugar diet; I.C.V., intracerebroventricular; PNN, perineuronal net; WFA, *Wisteria Floribunda* Lectin.



Extended Data Fig. 9 | See next page for caption.

Extended Data Fig. 9 | Neurofibrosis inhibition protective effects on metabolic disease are dependent upon insulin receptor expression in AgRP neurons. 12-week HFHS fed male C57BL/6 J mice received daily I.C.V. administration of vehicle or fluorosamine for 10 days and **a**) glucose tolerance, **b**) fasted blood glucose, **c**) fasted plasma insulin, **d**) HOMA-IR and **e**), **f**) insulin-induced p-AKT expression was assessed. Hyperinsulinemic-euglycaemic clamps were performed in HFHS fed mice following administration of fluorosamine daily for 5 days I.C.V. and **g**) GIR, **h**) glucose disposal, **i**) EGP, **j**) tissue specific insulin-stimulated uptake and **k**) body weight was determined. C57BL/6 J mice fed HFHS diet and treated with low dose STZ to phenocopy aspects of late stage T2D received daily I.C.V. administration of vehicle or fluorosamine for 14 days. **l**) Daily blood glucose and **m**) glucose tolerance was assessed. **n**) 12-week HFHS fed AgRP-Cas9 mice received bilateral injections of AAV-gScrambled or AAV-gIR. 12-week later mice received daily I.C.V. administered vehicle or fluorosamine for 10 days and **o**) body weights,

p) food intake, **q**) energy expenditure and **r**) glucose tolerance was assessed. Results are mean \pm SEM. Significance determined a, b, c, d, f, p-r) one-way ANOVA with Tukey's multiple comparisons, g, h, l, o) two-way ANOVA with multiple comparisons, and i, j, k, m) two-tailed t-tests. n = biologically independent samples and significance is representative of at least two independent experiments. Scale bar, 100 μ m. * = Vehicle to Fluorosamine 100 μ g, or AAV-gScrambled + Vehicle to AAV-gScrambled + Fluorosamine; # = Vehicle to Fluorosamine 250 μ g, or AAV-gScrambled + Fluorosamine to AAV-gIR + Fluorosamine, and \$ = AAV-gIR + Vehicle to AAV-gIR + Fluorosamine. #, \$, *p < 0.05; ##, **p < 0.01; ###, ***p < 0.001. *Abbreviations:* III, 3rd ventricle; AUC, area under curve; GIR, glucose infusion rate; HFHS, high-fat high-sugar diet; I.C.V., intracerebroventricular; IR, Insulin Receptor; p-AKT, AKT Ser-473 phosphorylation; PNN, perineuronal net; STZ, streptozotocin; WFA, *Wisteria Floribunda* Lectin.



Extended Data Fig. 10 | Intranasal administration of fluorosamine promotes weight loss through enhanced energy expenditure and satiety.

a) 12-week-old male C57Bl6/J mice received daily intranasal administration of a biotin-conjugated vehicle or fluorosamine (5 mg/animal) for 3 days and **b)** abundant fluorosamine-biotin expression was observed in the ARC. 12-week HFHS fed C57Bl6/J male mice received daily intranasal administration of vehicle or fluorosamine (1 or 5 mg/animal) for 14 days and **c, d)** adiposity, **e)** energy expenditure and **f)** ambulatory activity were assessed. Following 14 days of intranasally delivered vehicle or fluorosamine (1 or 5 mg/animal) mice were fasted overnight then given *ad libitum* access to food and **g)** behavior

(feeding, drinking, grooming, active, inactive, and resting) was monitored. **h)** The transition point from feeding to resting/satiety was assessed and **i)** the time to satiety was determined. Following 14 days of vehicle or fluorosamine treatment mice were administered insulin and brains processed for immunohistochemistry monitoring of **k, l)** insulin-induced p-AKT expression. Results are mean \pm SEM; significance determined using **c, d, i, j, l)** one-way ANOVA with Tukey's multiple comparisons and **e)** two-way ANOVA with repeated measures. n = biologically independent samples. **Abbreviations:** I.N., intranasal; ingWAT, inguinal adipose tissue; BAT, brown adipose tissue; epiWAT, epididymal adipose tissue; p-AKT, AKT Ser-473 phosphorylation.

Reporting Summary

Nature Portfolio wishes to improve the reproducibility of the work that we publish. This form provides structure for consistency and transparency in reporting. For further information on Nature Portfolio policies, see our [Editorial Policies](#) and the [Editorial Policy Checklist](#).

Statistics

For all statistical analyses, confirm that the following items are present in the figure legend, table legend, main text, or Methods section.

- | n/a | Confirmed |
|-------------------------------------|--|
| <input type="checkbox"/> | <input checked="" type="checkbox"/> The exact sample size (n) for each experimental group/condition, given as a discrete number and unit of measurement |
| <input type="checkbox"/> | <input checked="" type="checkbox"/> A statement on whether measurements were taken from distinct samples or whether the same sample was measured repeatedly |
| <input type="checkbox"/> | <input checked="" type="checkbox"/> The statistical test(s) used AND whether they are one- or two-sided
<i>Only common tests should be described solely by name; describe more complex techniques in the Methods section.</i> |
| <input checked="" type="checkbox"/> | <input type="checkbox"/> A description of all covariates tested |
| <input type="checkbox"/> | <input checked="" type="checkbox"/> A description of any assumptions or corrections, such as tests of normality and adjustment for multiple comparisons |
| <input type="checkbox"/> | <input checked="" type="checkbox"/> A full description of the statistical parameters including central tendency (e.g. means) or other basic estimates (e.g. regression coefficient) AND variation (e.g. standard deviation) or associated estimates of uncertainty (e.g. confidence intervals) |
| <input type="checkbox"/> | <input checked="" type="checkbox"/> For null hypothesis testing, the test statistic (e.g. F , t , r) with confidence intervals, effect sizes, degrees of freedom and P value noted
<i>Give P values as exact values whenever suitable.</i> |
| <input checked="" type="checkbox"/> | <input type="checkbox"/> For Bayesian analysis, information on the choice of priors and Markov chain Monte Carlo settings |
| <input checked="" type="checkbox"/> | <input type="checkbox"/> For hierarchical and complex designs, identification of the appropriate level for tests and full reporting of outcomes |
| <input type="checkbox"/> | <input checked="" type="checkbox"/> Estimates of effect sizes (e.g. Cohen's d , Pearson's r), indicating how they were calculated |

Our web collection on [statistics for biologists](#) contains articles on many of the points above.

Software and code

Policy information about [availability of computer code](#)

Data collection Olympus cellSens Dimension software v2.1, Zeiss ZEN v2.1, Leica Application Suite X, Sutterpatch software, Bruker OPUS 7.0 spectroscopy software, Sable Systems Macro Interpreter v23.6.0 and MetaScreen v2.3.15.13

Data analysis GraphPad Prism7 statistical analysis software, ImageJ v1.53s software, Sutterpatch software, Clampfit 10.7 software

For manuscripts utilizing custom algorithms or software that are central to the research but not yet described in published literature, software must be made available to editors and reviewers. We strongly encourage code deposition in a community repository (e.g. GitHub). See the Nature Portfolio [guidelines for submitting code & software](#) for further information.

Data

Policy information about [availability of data](#)

All manuscripts must include a [data availability statement](#). This statement should provide the following information, where applicable:

- Accession codes, unique identifiers, or web links for publicly available datasets
- A description of any restrictions on data availability
- For clinical datasets or third party data, please ensure that the statement adheres to our [policy](#)

Source data provided. The data that support the findings of this study are available from the corresponding authors upon request.

Research involving human participants, their data, or biological material

Policy information about studies with [human participants or human data](#). See also policy information about [sex, gender \(identity/presentation\), and sexual orientation](#) and [race, ethnicity and racism](#).

Reporting on sex and gender	N/A
Reporting on race, ethnicity, or other socially relevant groupings	N/A
Population characteristics	N/A
Recruitment	N/A
Ethics oversight	N/A

Note that full information on the approval of the study protocol must also be provided in the manuscript.

Field-specific reporting

Please select the one below that is the best fit for your research. If you are not sure, read the appropriate sections before making your selection.

Life sciences Behavioural & social sciences Ecological, evolutionary & environmental sciences

For a reference copy of the document with all sections, see [nature.com/documents/nr-reporting-summary-flat.pdf](https://www.nature.com/documents/nr-reporting-summary-flat.pdf)

Life sciences study design

All studies must disclose on these points even when the disclosure is negative.

Sample size	Sample sizes are indicated for each experiment and were chosen based on prior work by authors and according to standards in the field (examples of previous experimental techniques using similar or smaller sample sizes can be seen previously reported PMID: 30814586; PMID: 38378998; PMID: 38378998; PMID: 29670283; PMID: 30283080; PMID: 28377875; PMID: 25662011; PMID: 29670283; PMID: 32532984; PMID: 25626735). For immunostaining pilot data using the antibodies/staining to be quantified was conducted to provide an estimate of inter-subject variability.
Data exclusions	Due to variability across stereotaxic injections, only intraARC chABC or AAV treated animals that showed respective attenuated CSPG-ECM expression in the ARC or mCherry in the ARC were included. For HFHS+STZ mouse model only mice exhibiting stable blood glucose measurements of >15mM were included for experiments.
Replication	Each experiment was performed across several animals (numbers indicated in manuscript). Data from each individual animal is shown in the manuscript indicating the distribution of the results. Immunostaining for CSPG-ECM was confirmed across multiple independent experiments including different mouse strains, different mouse models of metabolic disease and in diverse species (mouse, rat). The effects of intraARC chondroitinase and intracerebroventricular fluorosamine treatment on metabolism have been recapitulated in at least 3 independent experiments and are demonstrated several times across the manuscript. For IHC 4 to 10 slices per individual animal were quantified and averaged for a data point.
Randomization	For all experiments random allocation was used for assignment of individual mice to different surgical and experimental groups.
Blinding	Experiments investigating the effects of intracerebroventricular fluorosamine treatment conducted with the operator blinded to treatment groups. Metabolic phenotyping and images were de-identified with the investigator performing quantifications blinded to the study groups. The analysis of CSPG-ECM expression was performed blinded to the effect on metabolism.

Reporting for specific materials, systems and methods

We require information from authors about some types of materials, experimental systems and methods used in many studies. Here, indicate whether each material, system or method listed is relevant to your study. If you are not sure if a list item applies to your research, read the appropriate section before selecting a response.

Materials & experimental systems

n/a	Involved in the study
<input type="checkbox"/>	<input checked="" type="checkbox"/> Antibodies
<input type="checkbox"/>	<input checked="" type="checkbox"/> Eukaryotic cell lines
<input checked="" type="checkbox"/>	<input type="checkbox"/> Palaeontology and archaeology
<input type="checkbox"/>	<input checked="" type="checkbox"/> Animals and other organisms
<input checked="" type="checkbox"/>	<input type="checkbox"/> Clinical data
<input checked="" type="checkbox"/>	<input type="checkbox"/> Dual use research of concern
<input checked="" type="checkbox"/>	<input type="checkbox"/> Plants

Methods

n/a	Involved in the study
<input checked="" type="checkbox"/>	<input type="checkbox"/> ChIP-seq
<input checked="" type="checkbox"/>	<input type="checkbox"/> Flow cytometry
<input checked="" type="checkbox"/>	<input type="checkbox"/> MRI-based neuroimaging

Antibodies

Antibodies used

Rabbit anti-aggrecan (1:1000, AB1031, Millipore, MA), chicken anti-GFP (1:2000; ab13970, Abcam, Cambridge, UK), Biotinylated HABP (1:100, 385911, Burlington, MA), rabbit anti-dsRed (1:2000, 600-401-379, Rockland, PA), rabbit anti-versican (1:1000, AB1033, Millipore, MA), biotinylated WFL (1:2000, L1516; Sigma-Aldrich, MO), rabbit anti-p-AKT (Ser-473) (1:300, 4060, Cell Signaling Technology, Beverly, MA), WFL-FITC (1:2000, FL-1351-2, Vector Laboratories, CA), Tenascin-C (1:500, M1-B4, Developmental Studies Hybridoma Bank, Iowa), HAPLN1 (1:500, 9/30/8-A-4, Developmental Studies Hybridoma Bank, Iowa), neurocan (1:300, 1F6-S, Developmental Studies Hybridoma Bank, Iowa), phosphacan (1:300, 3F8, Developmental Studies Hybridoma Bank, Iowa), brevican (1:500, 610895, BD Transduction Laboratories), guinea pig anti AgRP (1:500, AS506, Antibodies Australia, Melbourne, AUS), goat anti-chicken Alexa Fluor 488 (1:1000, ab150169, Abcam, Cambridge, UK), goat anti-rabbit Alexa Fluor-488, 595, 647 (1:1000, ab150077, ab150080, ab150083, Abcam, Cambridge, UK), Alexa Fluor 594, 647 Streptavidin (1:1000, 405240, BioLegend, CA), rabbit anti-UCP-1 (1:1000; ab10983, Abcam, Cambridge, UK), goat anti-rabbit Alexa Fluor 488 (1:1000, ab150077, Abcam, Cambridge, UK), rabbit anti-p-AKT (Ser-473) (1:300; #4060, Cell Signaling Technology, Beverly, MA), goat anti-rabbit Alexa Fluor 647 (1:1000, ab150083, Abcam, Cambridge, UK) or biotinylated goat anti-rabbit (1:1000, BA-1000, Vector Laboratories, CA). p-STAT3 (Tyr705) (1:500; #9131S, Cell Signaling Technology, Beverly, MA)

Validation

All primary antibodies have been previously used by authors and in several publications. Citation numbers determined from CiteAb unless otherwise specified.

- rabbit anti-aggrecan (1:1000, AB1031, Millipore, MA): cited 211 times, validated for IF, IH(P), IP, WB & other. https://www.merckmillipore.com/AU/en/product/Anti-Aggrecan-Antibody,MM_NF-AB1031
- chicken anti-GFP (1:2000; ab13970, Abcam, Cambridge, UK): cited 4257 times, validated for WB, ICC/IF. <https://www.abcam.com/products/primary-antibodies/gfp-antibody-ab13970.html>
- Biotinylated HA (1:100, 385911, Millipore, MA): cited 148 times, validated for ELISA, ICC/IF. https://www.merckmillipore.com/AU/en/product/Hyaluronic-Acid-Binding-Protein-Bovine-Nasal-Cartilage-Biotinylated,EMD_BIO-385911#overview
- rabbit anti-dsRed (1:2000, 600-401-379, Rockland, PA): cited 1333 times, validated for WB, ELISA, IHC, IF, FC, EM, FISH, IP, Multiplex & other. <https://www.rockland.com/categories/primary-antibodies/rfp-antibody-pre-adsorbed-600-401-379/>
- rabbit anti-versican (1:1000, AB1033, Millipore, MA): cited 62 times, validated for IH, IF, IP, WB. <https://www.sigmaaldrich.com/AU/en/product/mm/ab1033>
- biotinylated WFA (1:2000, L1516; Sigma-Aldrich, MO), cited 54 times on manufacturer website, validated for IHC/IF. <https://www.sigmaaldrich.com/AU/en/product/sigma/l1516>
- rabbit anti-p-AKT (Ser-473) (1:300, 4060, Cell Signaling Technology, Beverly, MA). Cited 10,713 times, validated for WB, IP, IHC, IF. <https://www.cellsignal.com/products/primary-antibodies/phospho-akt-ser473-d9e-xp-174-rabbit-mab/4060>
- WFA-FITC (1:2000, FL-1351-2, Vector Laboratories, CA). Cited 89 times on manufacturer website, validated for IHC/IF. <https://vectorlabs.com/products/fluorescein-wisteria-floribunda-lectin>
- Tenascin-C (1:500, M1-B4, Developmental Studies Hybridoma Bank, Iowa). Cited 52 times, validated for IHC, IF, ICC, WB, Elisa. <https://dshb.biology.uiowa.edu/M1-B4>
- HAPLN1 (1:500, 9/30/8-A-4, Developmental Studies Hybridoma Bank, Iowa). Cited 38 times, validated for IHC, IP, WB. <https://dshb.biology.uiowa.edu/9-30-8-A-4>
- neurocan (1:300, 1F6-S, Developmental Studies Hybridoma Bank, Iowa). Cited 30 times, validated for IHC & WB. <https://dshb.biology.uiowa.edu/1F6>
- phosphacan (1:300, 3F8, Developmental Studies Hybridoma Bank, Iowa). Cited 32 times, validated for IHC & WB. <https://dshb.biology.uiowa.edu/3F8>
- brevican (1:500, 610895, BD Transduction Laboratories). Cited 20 times, validated for IHC & WB. <https://www.bdbiosciences.com/en-au/products/reagents/microscopy-imaging-reagents/immunofluorescence-reagents/purified-mouse-anti-brevican.610895>
- guinea pig anti AgRP (1:500, AS506, Antibodies Australia, Melbourne, AUS), validated for IHC in house in conjunction with reporter lines and KO models. Validated for IHC in several publications including PMID: 30995667; PMID: 21418339.
- goat anti-chicken Alexa Fluor 488 (1:1000, ab150169, Abcam, Cambridge, UK). Cited 213 times, validated for IHC, IF, ICC, Elisa & others. <https://www.abcam.com/products/secondary-antibodies/goat-chicken-igy-hl-alex-fluor-488-ab150169.html>
- goat anti-rabbit Alexa Fluor-488, 595, 647 (1:1000, ab150077, ab150080, ab150083, Abcam, Cambridge, UK). Cited 3358 times, validated for IHC, Flow, ICC/IF & others. <https://www.abcam.com/en-au/products/secondary-antibodies/goat-rabbit-igg-h-l-alex>

fluor-488-ab150077

- goat anti-rabbit Alexa Fluor-595 (1:1000, ab150080, Abcam, Cambridge, UK). Cited 708 times, validated for WB, IHC, ICC/IF & others. <https://www.abcam.com/en-au/products/secondary-antibodies/goat-rabbit-igg-h-l-alex-fluor-594-ab150080>
- goat anti-rabbit Alexa Fluor-647 (1:1000, ab150083, Abcam, Cambridge, UK). Cited 188 times, validated for IHC, Flow, ICC/IF & others. <https://www.abcam.com/en-au/products/secondary-antibodies/goat-rabbit-igg-h-l-alex-fluor-647-preadsorbed-ab150083>
- Alexa Fluor 594, 647 Streptavidin (1:1000, 405240, BioLegend, CA). Cited 9 times on manufacturer website, validated for ICC/IF, IHC & others. <https://www.biolegend.com/fr-ch/products/alex-fluor-594-streptavidin-9707>
- rabbit anti-UCP-1 (1:1000; ab10983, Abcam, Cambridge, UK). Cited 865 times, validated for WB, IHC/IF. <https://www.abcam.com/en-au/products/primary-antibodies/ucp1-antibody-ab10983>
- goat anti-rabbit Alexa Fluor 488 (1:1000, ab150077, Abcam, Cambridge, UK). Cited 3348 times, validated for IHC, ICC/IF, Elisa & others. <https://www.abcam.com/en-au/products/secondary-antibodies/goat-rabbit-igg-h-l-alex-fluor-488-ab150077>
- rabbit anti-p-AKT (Ser-473) (1:300; #4060, Cell Signaling Technology, Beverly, MA). Cited 10713 times, validated for WB, IHC, ICC/IF & others. <https://www.cellsignal.com/products/primary-antibodies/phospho-akt-ser473-d9e-xp-174-rabbit-mab/4060>
- biotinylated goat anti-rabbit (1:1000, BA-1000, Vector Laboratories, CA). Cited 3695 times, validated for IHC, ICC/IF, WB & others. <https://vectorlabs.com/products/biotinylated-goat-anti-rabbit-igg>
- p-STAT3 (Tyr705) (1:500; #9131S, Cell Signaling Technology, Beverly, MA). Cited 1473 times, validated for WB, IHC & others. <https://www.cellsignal.com/products/primary-antibodies/phospho-stat3-tyr705-antibody/9131>

Eukaryotic cell lines

Policy information about [cell lines and Sex and Gender in Research](#)

Cell line source(s)	HEK293T: source Sigma
Authentication	Authenticated by manufacturer (https://www.sigmaldrich.com/AU/en/product/sigma/cb_12022001)
Mycoplasma contamination	Not tested for mycoplasma contamination
Commonly misidentified lines (See ICLAC register)	N/A

Animals and other research organisms

Policy information about [studies involving animals; ARRIVE guidelines](#) recommended for reporting animal research, and [Sex and Gender in Research](#)

Laboratory animals	C57BL/6J mice (male, aged 8-22 weeks), db/db mice(male 8-14 weeks), Npy-GFP mice (male, 8-20 weeks), Pomc-GFP mice (male, 8-20 weeks), NZO mice (male, 8-20weeks), AgRP-Cas9 mice (male, 8-22 weeks), Sprague Dawley rats (8-24 weeks).
Wild animals	The study did not involve use of wild animals
Reporting on sex	All experiments were performed on male mice and are specified in methods and results.
Field-collected samples	The study did not involve use of field-collected samples
Ethics oversight	Experiments were approved by The University of Melbourne, Monash University and St Vincents Research Institutes Animal Ethics Committee (10323, 10324, 10352, 10385, 10427, 21712, 22282, 22404, 25349, 28097).

Note that full information on the approval of the study protocol must also be provided in the manuscript.

Plants

Seed stocks	N/A
Novel plant genotypes	N/A
Authentication	N/A